

Contents lists available at ScienceDirect

Journal of the Mechanics and Physics of Solids

journal homepage: www.elsevier.com/locate/jmps



Mechanical performance of additively-manufactured anisotropic and isotropic smooth shell-lattice materials: Simulations & experiments



Colin Bonatti^{a,b}, Dirk Mohr^{a,*}

^a Department of Mechanical and Process Engineering, Swiss Federal Institute of Technology (ETH), Zurich, Switzerland

^b Impact and Crashworthiness Laboratory, Department of Mechanical Engineering, Massachusetts Institute of Technology, Cambridge, MA, USA

ARTICLE INFO

Article history:

Received 23 October 2017

Revised 15 August 2018

Accepted 21 August 2018

Available online 31 August 2018

Keywords:

Mechanical metamaterials

Architected materials

Unit cell analysis

Shell-lattices

Stiffness

Energy absorption

ABSTRACT

A novel family of smooth-shell structures is introduced as mechanical metamaterials of exceptional specific energy absorption capacity. The proposed shell structures respect all symmetries of the face-centered cubic crystal. To obtain a smooth curvature shell structure, the exact shape of the shell mid-plane is determined through the minimization of a bending-energy based measure of the overall curvature. Among the members of this new family, the mechanical properties of a Triply Periodic Minimal Surface (TPMS)-like architecture and an elastically-isotropic derivate are investigated in detail. The TPMS-like structure showed important anisotropy in both its small and large strain responses, with loading-direction dependent differences in stiffness of more than 100%. The mechanical properties of the elastically-isotropic shell-lattice turned out to be close to the mean value for all directions of loading for the TPMS-like structures. For relative densities ranging from 1% to 50%, the shell-lattices always exhibited a higher mechanical performance than truss-lattices of equal density. For relative densities greater than 20%, the mechanical response of the shell-lattices is more stable than that of truss-lattices which makes them particularly suitable as higher order structures in hierarchical metamaterial design. The computational results are partially confirmed through compression experiments on additively-manufactured stainless steel specimens. A direct comparison of the stress-strain curve of additively-manufactured stainless steel 316L with that of sheets made from the same alloy revealed an increase in yield strength of about 30% related to the selective laser melting process.

© 2018 Elsevier Ltd. All rights reserved.

1. Introduction

Enabled by the accelerated development of additive manufacturing techniques at small length scales, the past few years have seen a surge of interest in novel architected materials with man-designed internal structure. As discussed in the review by Xiong et al. (2015), those metamaterials have the potential to bring innovation to a variety of fields, for example as constituent material of ultra-light mechanical energy absorbers, high performance heat exchangers, or bio-medical implants.

* Corresponding author.

E-mail address: mohr@mit.edu (D. Mohr).

In the scientific literature, much attention is paid to the scaling of the mechanical properties of metamaterials with relative density. Deshpande et al. (2001b) showed that stretching-dominated truss-lattice materials present near-linear scaling of elastic moduli and initial yield strength, superior to that of stochastic bending-dominated metamaterials such as foams. Perhaps the best-known example is the octet-truss, of which Deshpande et al. (2001a) investigated the elastic and failure response both experimentally and analytically. The octet-truss's properties have been widely studied, including its macroscopic plastic behavior (Mohr, 2005), fracture toughness (O'Masta et al., 2017) and buckling-to-yield failure transition (Carlton et al., 2017). Elsayed and Pasini (2010) elaborated design maps for octet-truss-inspired lattices with simultaneous yield and buckling limits. This accumulated knowledge as well as its popularity make the octet-truss a reference architecture for truss-lattice materials. For example, scale effects in octet truss lattices made from copper with strut diameters of a few microns have been investigated by Wendy Gu and Greer (2015), while He et al. (2017) made use of molecular dynamics simulations in conjunction with theoretical models to assess the compressive response of copper nano-lattices with strut diameters of a few nanometers only, reporting significant property enhancement as compared to bulk copper.

The linear scaling of the mechanical properties of the octet truss-lattice breaks down at low relative densities due to buckling instabilities (Deshpande et al., 2001a). This issue has been partially addressed by the design of hierarchical metamaterials which feature different levels of structure (e.g. Meza et al., 2015; Zheng et al., 2016). Hierarchical design allows extremely low relative densities to be reached for the overall structure while keeping mesostructural feature-level aspect ratios low enough to retard instability-driven failure. By hierarchically combining octahedral and octet-trusses, Meza et al. (2015) have been able to achieve the linear-scaling of the elastic and elastic limit properties down to relative densities of about 10^{-4} .

The optimality of scaling laws for truss-lattices is not only limited by early instability failure. The motifs used at the different hierarchical levels are themselves often far from optimal from a mechanical point of view, in particular when high performance is sought with regards to specific energy absorption under large compressive strains. Closed-cell plate-lattice materials with polyhedral mesostructures have been shown to present far better elastic properties than their beam-based, open-cell counterparts of the same weight (Berger et al., 2017; Tancogne-Dejean et al., 2018c). However, those structures are still problematic from a manufacturing point-of-view, as their closed-cell nature prevents the use of liquid-bath or powder-bed based techniques, while direct deposition techniques are challenged by the construction of unsupported cell walls.

Another emerging category of metamaterial architectures next to truss- and plate-lattices are shell-lattices, i.e. periodic structures composed of non-intersecting shells (e.g. Han et al., 2015). These open cell shell structures have the particularity of separating two fluid phases. This feature facilitates their production through additive manufacturing techniques that require the extraction of powder or liquids. Moreover, it makes them suitable for applications requiring multi-functionality such as mechanical resistance combined with heat exchange capability. Such surfaces naturally emerge in block copolymers where two macromolecules arrange at equilibrium by forming cocontinuous domains (e.g. Thomas et al., 1988). Constant mean-curvature surfaces, including Triply Periodic Minimal Surfaces (TPMS), and (mathematically simpler) level-set surfaces have been proposed as an approximation to the separating surface (e.g. Lambert et al., 1996). Following from those findings, cocontinuous composites, i.e. two-phase composites wherein each phase occupies the volume on one of the two sides of the limiting surface, have been proposed and their mechanical properties studied for a range of constituent materials.

Maldovan et al. (2007) studied the stiffness of microframes (solid/air composites) with several interface topologies, including some defined by level-set surfaces approximating the Schwarz P, I-WP and F-RD surfaces. Wang et al. (2011) used the same geometries to print glassy polymer/rubbery polymer composites, where the volume fraction of the respective phases was varied leveraging one degree of freedom in the level set function. They reported enhanced properties as compared to particle-reinforced composites, including increased damage tolerance. Topologically similar carbon/epoxy bicontinuous composites were produced by Lee et al. (2012) via a combination of 3D direct laser writing, pyrolysis and infiltration, and revealed to present specific energy absorptions of up to 720 kJ/kg. A similar approach consists in reinforcing a soft matrix through a uniform-thickness shell with the analytical surface as a mid-surface instead of using "skeletal" truss-structures. Abueidda et al. (2015) analyzed numerically the thermal expansion of such cocontinuous composites, revealing a low coefficient of thermal expansion of interest for applications. Dalaq et al. (2016a,b) studied numerically and experimentally the elastic modulus, strength, strain at failure and toughness of such composites (with varying TPMSs) consisting of a Tango-Plus matrix reinforced by TPMS-shaped Vero-Plus.

Foam-like shell-lattice materials can be obtained by retaining only the non-intersecting shell structures of uniform thickness. With the goal of identifying superior scaffold designs for tissue engineering, Kapfer et al. (2011) designed such shell-lattices and estimated their elastic properties, as well as their fluid permeability, numerically and compared those to TPMS-based skeletal networks of the same porosity, revealing superior mechanical properties. Han et al. (2015) proposed ultra-low density shell-lattices consisting of Schwarz P- and Schwarz D-surfaces. They optimized these structures for stiffness along one direction by reducing the nozzle size between neighboring cells while breaking down the cubic symmetry by elongating the unit-cell along the direction. Lee et al. (2017) investigated the stiffness and yield properties of shell-lattices based on the Schwarz-P minimal surface. Al-Ketan et al. (2017) studied the compressive behavior of steel-based BCC metamaterials, including a BCC truss-lattice, and shell-lattice structures based on a level-set approximation of the I-WP TPMS. They showed that the shell-lattice presented superior mechanical properties as compared to the truss-lattices. Bobbert et al. (2017) fabricated sixteen types of TPMS shell-lattices from Ti-6Al-4V, reporting low elastic properties, high strength, high fatigue resistance, and high permeability, thereby mimicking the properties of trabecular bone.

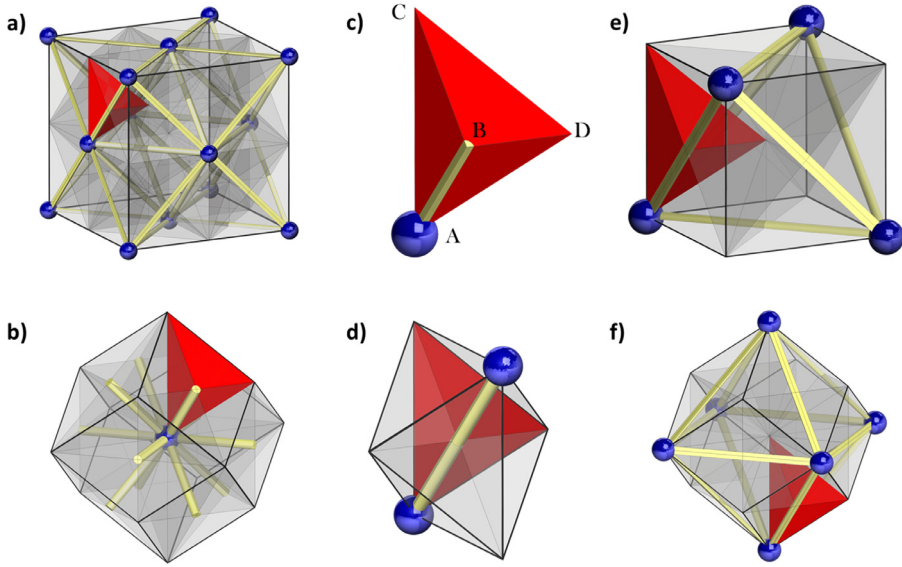


Fig. 1. Selected decompositions of the FCC geometry. Blue spheres represent the nodes of the lattice, yellow bars represent the links between closest-neighbor nodes. (a) cubic unit-cell, (b) rhombic dodecahedral unit-cell, (c) fundamental tetrahedron, (d) irregular octahedron obtained by collecting all fundamental tetrahedra resting on a midpoint between next-neighbor nodes, (e) cube obtained by collecting all fundamental tetrahedra resting on a tetrahedral site of the lattice, (f) rhombic dodecahedron obtained by collecting all tetrahedra resting on an octahedral site of the lattice. (For interpretation of the references to color in this figure legend, the reader is referred to the web version of this article.)

A common feature of most truss- shell- and plate-lattice materials is that their elasto-plastic mechanical response depends on the orientation of the loading with respect to their planes of symmetry. The comparison of their mechanical properties therefore needs to be done with utmost care. For example, the Young's modulus of truss-lattices of BCC symmetry may vary by two orders of magnitude (Tancogne-Dejean and Mohr, 2018a) since the same structure may change its response from stretching- to bending-dominated as a function of the loading direction. In the present work, we characterize the loading direction dependency of the stiffness, yield strength and energy absorption capability of a TPMS-like shell-lattice for comparison with the octet truss-lattice. A special curvature-based cost-function is used to generate the TPMS-like structures. It is subsequently tailored such as to obtain an elastically-isotropic shell-lattice. This allows for the ranking of the stiffness and yield strength of shell-lattices with respect to that of elastically-isotropic plate-lattices (Berger et al., 2017), elastically-isotropic tube-lattices (Tancogne-Dejean and Mohr 2018b) and elastically-isotropic truss-lattices (Gurtner and Durand, 2014). Experiments are performed on specimens made from stainless steel 316 L using selective laser melting to validate the numerical findings. In addition, the experimental results confirm the recently-discovered potential of additive manufacturing (Wang et al., 2018) to create microstructures of superior strength than conventional processing routes for the same alloy.

2. Shell-lattices of cubic symmetry

A new family of shell-lattices is obtained through the smoothening of the geometry of hollow FCC trusses. We begin by discussing the fundamental domain of FCC metamaterials before introducing a bending-energy inspired potential function to define smooth shell structures.

2.1. Description of FCC metamaterials

Consider the set S of linear transformations that preserve the set of nodes of a Face-Centered Cubic (FCC) lattice. If the spatial distribution of matter in a periodic medium remains invariant for all linear transformations $T_i \in S$, the medium is referred to as "FCC metamaterial". In order to efficiently describe FCC metamaterials, different decompositions of the FCC lattice are of interest:

- **The cubic unit-cell.** Fig. 1a presents a unit-cell of the FCC lattice with the nodes shown in blue, and the line segments joining closest-neighbors shown in yellow. Once the unit-cell of an FCC metamaterial is defined, the periodic lattice is obtained by translations along the edges of the cubic unit-cell. The cubic unit-cell contains four nodes of the FCC lattice (eight eighth-nodes at the unit-cell corners, and six half-nodes on the unit-cell faces).
- **The rhombic dodecahedral unit-cell.** The elementary unit-cell for creating an FCC metamaterial through translations only, takes the form of a rhombic dodecahedron centered around a single node of the lattice (Fig. 1b). The rhombic dodecahedron is the smallest volume containing all the geometric information necessary for computing the homogenized mechanical behavior of periodic FCC metamaterials.

- **The fundamental tetrahedron.** Taking into account the full set of FCC symmetries (including rotations and mirror transformations in addition to translations), a tetrahedron can be identified as the fundamental domain defining a periodic FCC metamaterial (Fig. 1c). Fig. 1a and b show how the fundamental tetrahedron (shown in red) integrates into the cubic and the rhombic dodecahedral unit-cells, respectively. In Fig. 1c, the four vertices of the fundamental tetrahedron are identified by letters. Vertex A is the only vertex that is situated at a node of the FCC lattice. Vertex B is located at the mid-point between two first neighbors of the FCC lattice, vertex C is situated at an octahedral site and vertex D lies on a tetrahedral site of the FCC lattice. Using Miller notations to describe the FCC lattice directions, we note that the edges [AB] and [BC] are aligned with the [110] direction, [AC] and [BD] are aligned with the [100] direction, and [AD] and [CD] are aligned with the [111] direction. The full FCC metamaterial is then obtained as a collection of copies of this fundamental tetrahedron, each of them translated, mirrored and rotated into a particular configuration.
- Other useful substructures of the FCC lattice are obtained when considering all fundamental tetrahedra around the vertices B, C and D. The collection of all fundamental tetrahedra around the tetrahedral site D form a cube that features eighth nodes at four of the eight cube corners (Fig. 1d). Different from the cubic unit-cell described above, the entire FCC structure cannot be composed through translations only when using the smaller cubic cell obtained from collecting all fundamental tetrahedra around a tetrahedral sites of the FCC lattice. Another rhombic dodecahedral unit-cell is formed by the collection of all fundamental tetrahedra around vertex C (Fig. 1e), while an octahedron is formed by all fundamental tetrahedra around vertex B (Fig. 1f).

Illustrations of the resulting FCC metamaterials for different motifs included in the fundamental tetrahedron are shown in Fig. 2. In the case of struts placed on the edges of the tetrahedron, the widely-studied octet truss (FCC) lattice structure is obtained when positioning a straight strut along the edge [AB] (Fig. 2a), or equivalently along edge [BC] (Fig. 2d), while a skeletal rhombic dodecahedron (RD) truss lattice is obtained by selecting the opposing edges ([CD] and [AD], Fig. 2f and 2c). A simple cubic structure is obtained when positioning a straight strut either along the edge [AC] (Fig. 2b) or edge [BD] (Fig. 2e).

2.2. Smooth shell-lattices

An exploratory study (Bonatti and Mohr, 2017) on the large deformation response of basic FCC metamaterials revealed that plastic deformation often localizes at corners and non-smooth intersections (Fig. 3), instead of distributing the plastic dissipation in a uniform manner throughout the entire structure. The apparent correlation between concentrations in deformation and “concentrations of curvature” triggered the present design of a smooth shell structure of nearly uniform curvature. The idea is to design a porous FCC metamaterial by embedding a smooth curvature shell surface in the fundamental tetrahedron.

- **Boundary conditions.** The shell structure of the hollow octet truss lattice, which rests on all four faces of the fundamental tetrahedron (Fig 4a), is taken as starting point. The defining surface Ω of a smooth shell-lattice shall rest on the faces (opposite to vertex) A, B, C and D of the fundamental tetrahedron, in that order and with no hole, separating the tetrahedron into two volumes with edge [AB] on one side and edge [CD] on the other. The intersections with the tetrahedron's faces (which correspond to the borders of the surface) are submitted to orthogonality to the face they lie on, in order to ensure smooth connections (C_1 -continuity) after applying the mirror transformations required to recreate the FCC lattice material. Recall from Fig. 2 that the octet truss lattice structure is obtained by placing a strut along the edge [AB] of the fundamental tetrahedron, while placing a strut along the edge [CD] yields a skeletal rhombic dodecahedron. Similar to the F-RD (FCC-Rhombic Dodecahedron) minimal surface, the structures defined herein will be generated by a surface that can at the same time be seen as a smoothed hollow-truss FCC network (see Fig. 4c), and a smoothed hollow-truss RD network (see Fig. 4d). The exact shape of the motif inside the fundamental tetrahedron of the novel smooth shell structure (Fig. 4b) is determined by the choice of a functional that will be minimized.
- **Basic functional.** We choose to minimize the surface integral

$$\int_{\Omega} (k_1^2 + k_2^2)^2 dA \quad (1)$$

with k_1 and k_2 the principal curvatures at any given point on the surface Ω . It is noted that the integrant has an interpretation in mechanics: for an elastic material of zero Poisson's ratio, it represents the square of the strain energy required to bend an initially flat platelet into the shape of the smooth shell surface.

- **Biased functional.** In a second step, a degree of freedom is introduced, which gives priority to curvature “along” one truss-lattice (FCC or RD) over the other. In order to effectively do this, two directions on the surface are taken as representative of the direction of the truss. The direction “along the FCC lattice” at point \mathbf{x} on the surface is taken as the intersection of the surface and plane P , where P is the plane containing \mathbf{x} and edge [AB] of the tetrahedron. It is represented by its direction vector at \mathbf{x}, \mathbf{e}_F . Conversely the direction “along the RD lattice” at point \mathbf{x} on the surface is taken as the intersection of the surface and plane P , where P is the plane containing \mathbf{x} and edge [CD] of the tetrahedron, and is modeled by its direction vector at \mathbf{x}, \mathbf{e}_R . To introduce a bias in the measure of the integrand, the respective weights of curvatures along those directions are modulated by a scalar parameter. In order to effect this Eq. (1) can be rewritten as

$$\int_{\Omega} Tr(A^2)^2 dA \quad (2)$$

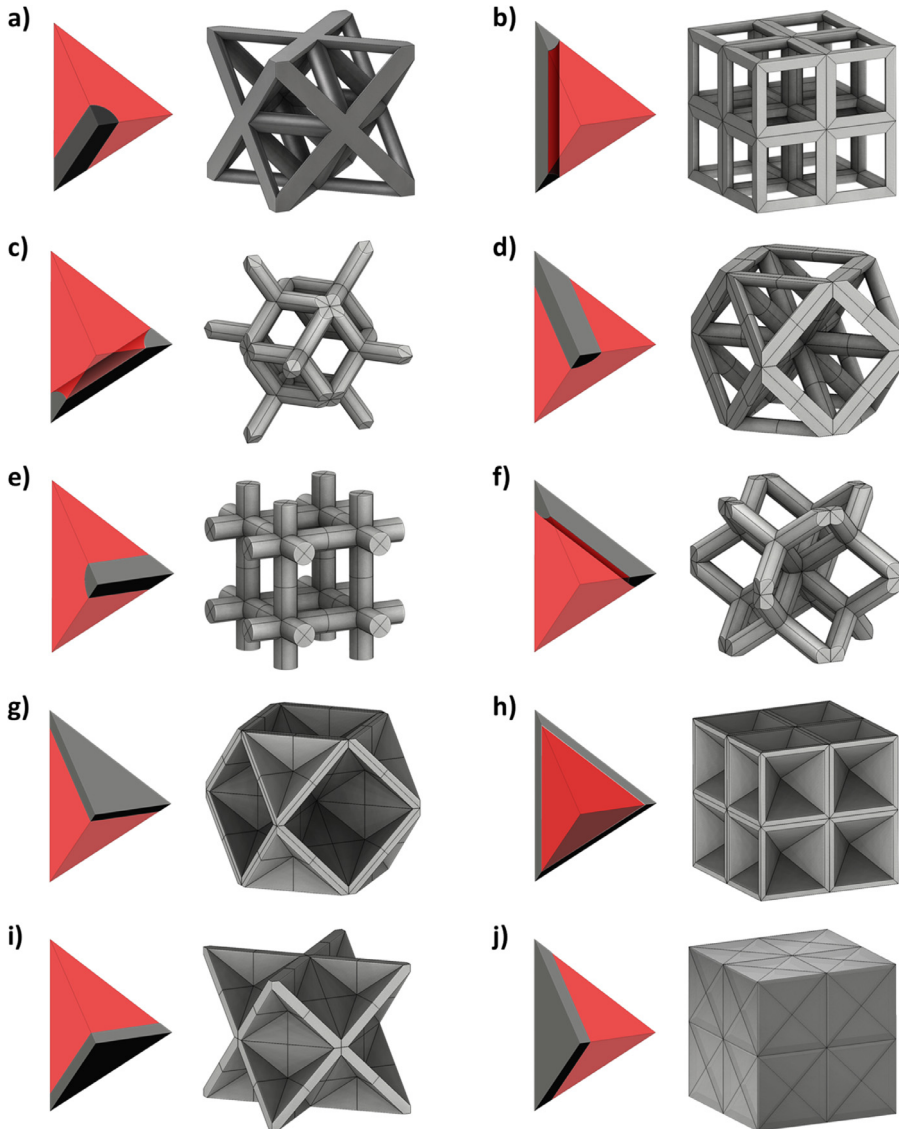


Fig. 2. Resulting FCC metamaterial architectures for different motifs included in the fundamental tetrahedron: (a) edge AB → octet-truss, (b) edge AC → simple cubic truss, (c) edge AD → rhombic dodecahedron truss, (d) edge BC → octet-truss, (e) edge BD → simple cubic truss, (f) edge CD → rhombic dodecahedron truss, (g) surface A → rhombic dodecahedral foam, (h) surface B → foam with irregular-octahedral cells, (i) surface C → rhombic dodecahedral foam, (j) surface D → simple cubic foam.

where A is the matrix of the shape operator of the surface at \mathbf{x} , expressed in basis $\{\mathbf{e}_F, \mathbf{e}_R\}$. The new cost function is:

$$\int_{\Omega} Tr \left(\left(\begin{bmatrix} \sqrt{\beta} & 0 \\ 1 & 1 \end{bmatrix} \cdot A \cdot \begin{bmatrix} \sqrt{\beta} & 0 \\ 1 & 1 \end{bmatrix} \right)^2 \right)^2 dA \quad (3)$$

where β is a scalar parameter controlling the bias and a value $\beta = 1$ corresponds to the unbiased functional (1).

The minimization problem defining the surface geometry is solved approximately using an in-house Matlab script. Firstly, a 2D square mesh is defined and projected into the fundamental tetrahedron (Fig 4b). First order derivatives, surface normal and curvatures are estimated using a finite difference scheme. The obtained approximation of the cost-function is then minimized by alternating between a Nelder–Mead algorithm and a gradient-descent. Solutions are obtained for values of β ranging from 0.2 to 5, defining a new family of shell-lattices.

Examples of the smooth structures are shown in Fig. 4c–d for different values of β . For low values of β (see Fig. 4c $\beta = 0.2$) curvature around the [AB] axis is penalized and the surface wraps around the [CD] axis – the generated structure resembles a smoothed RD truss-lattice. For high β values (see Fig. 4f, $\beta = 5$), the opposite happens and the structure

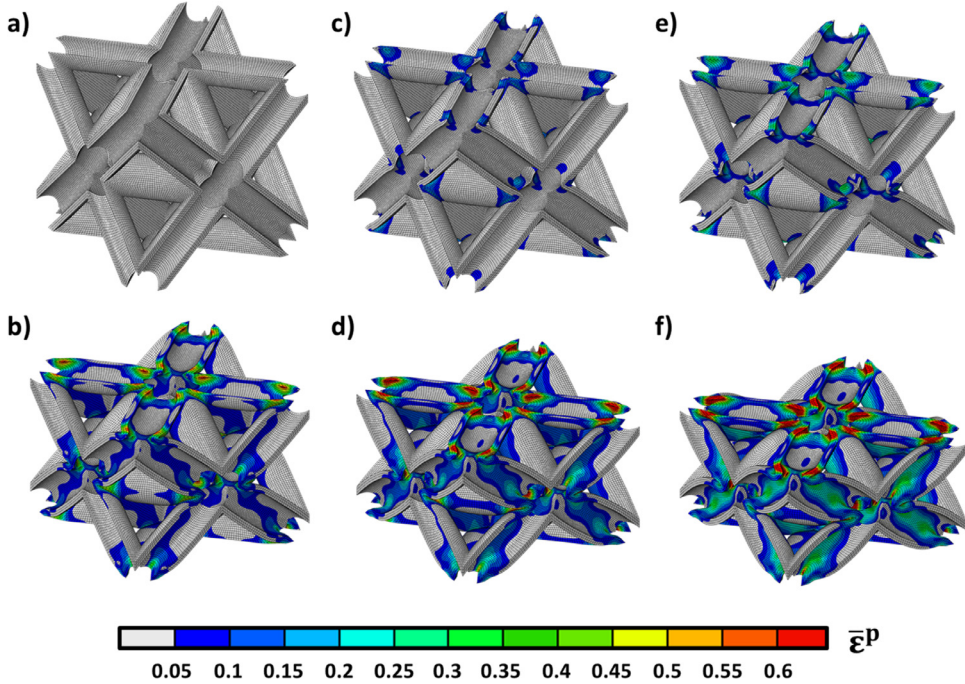


Fig. 3. View of equivalent plastic strain distributions on unit-cells of a hollow octet-truss structure at relative density $\bar{\rho} = 0.2$ studied in Bonatti and Mohr (2017), under uniaxial compression along [100] and for compressive engineering strains of 0, 5, 10, 20, 30, 40% respectively. The color-code shows concentration of plastic dissipation around the sharp edges at the nodes. (For interpretation of the references to color in this figure legend, the reader is referred to the web version of this article.)

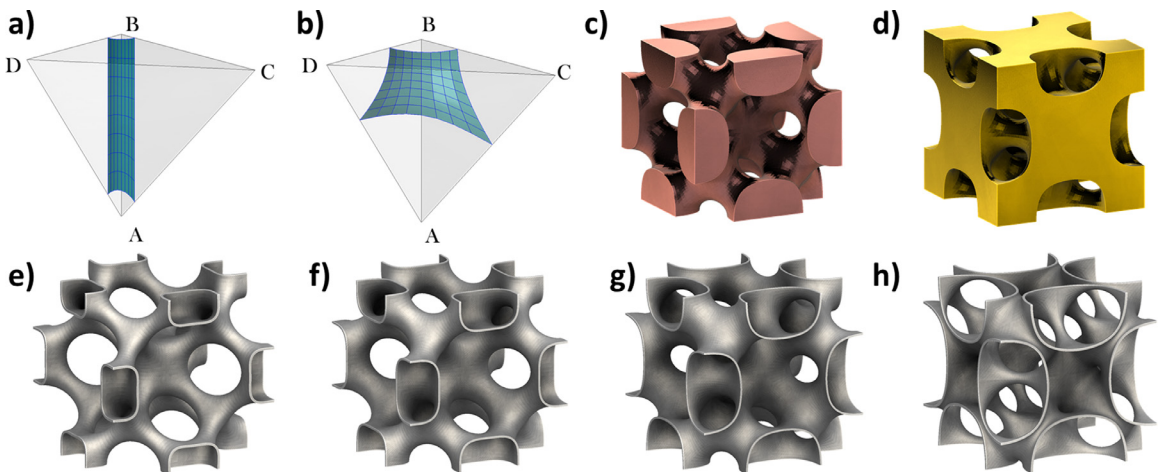


Fig. 4. Proposed smooth shell-lattice architecture: (a) shell structure inside the fundamental tetrahedron used as initial guess (hollow octet-truss), (b) double-curvature surface solution for $\beta = 1$, (c) RD fluid phase for $\beta = 1$, (d) FCC fluid phase for $\beta = 1$, (e) unit-cell for $\beta = 0.2$, (f) unit-cell for $\beta = 0.375$ ("iso-shell"), (g) unit-cell for $\beta = 1$ (TPMS-like), (h) unit-cell for $\beta = 5$.

resembles a smoothed octet-truss. The corresponding mesh coordinates for $\beta = 1$ are given in Table 1. The $\beta = 1$ solution, corresponding to an unbiased functional, is shown in Fig. 4e. The fluid volumes separated by it have equal volume, and it resembles the TPMS alternative (Schoen F-RD). As a matter of fact, their mechanical properties are also very similar (see Appendix).¹ In the sequel, the structure obtained for $\beta = 1$ will thus be referred to as "TPMS-like" shell-lattice.

¹ The only minor difference worth noting is that the bending-energy inspired smooth shell structure distributes stresses more uniformly, which is a potential advantage in fatigue-critical applications.

Table 1

Coordinates of approximate solution on the 9×9 node grid presented in Fig. 4b.

	1	2	3	4	5	6	7	8	9
1	[0.0000]	[0.0463]	[0.0922]	[0.1366]	[0.1781]	[0.2149]	[0.2442]	[0.2633]	[0.2696]
	[1.0000]	[1.0000]	[1.0000]	[1.0000]	[1.0000]	[1.0000]	[1.0000]	[1.0000]	[1.0000]
	[0.2328]	[0.2328]	[0.2225]	[0.2044]	[0.1781]	[0.1436]	[0.1012]	[0.0524]	[0.0000]
2	[0.0000]	[0.0468]	[0.0929]	[0.1376]	[0.1794]	[0.2165]	[0.2465]	[0.2665]	[0.2743]
	[0.9559]	[0.9596]	[0.9620]	[0.9631]	[0.9626]	[0.9604]	[0.9561]	[0.9497]	[0.9411]
	[0.2388]	[0.2352]	[0.2244]	[0.2059]	[0.1794]	[0.1447]	[0.1021]	[0.0530]	[0.0000]
3	[0.0000]	[0.0482]	[0.0953]	[0.1406]	[0.1832]	[0.2215]	[0.2533]	[0.2761]	[0.2880]
	[0.9119]	[0.9192]	[0.9241]	[0.9262]	[0.9253]	[0.9208]	[0.9123]	[0.8994]	[0.8822]
	[0.2480]	[0.2424]	[0.2300]	[0.2105]	[0.1832]	[0.1480]	[0.1049]	[0.0549]	[0.0000]
4	[0.0000]	[0.0507]	[0.0993]	[0.1459]	[0.1899]	[0.2302]	[0.2650]	[0.2922]	[0.3104]
	[0.8678]	[0.8788]	[0.8861]	[0.8893]	[0.8879]	[0.8813]	[0.8684]	[0.8490]	[0.8234]
	[0.2636]	[0.2547]	[0.2397]	[0.2183]	[0.1899]	[0.1538]	[0.1097]	[0.0581]	[0.0000]
5	[0.0000]	[0.0542]	[0.1051]	[0.1536]	[0.1997]	[0.2428]	[0.2817]	[0.3146]	[0.3410]
	[0.8238]	[0.8384]	[0.8481]	[0.8524]	[0.8505]	[0.8417]	[0.8245]	[0.7987]	[0.7645]
	[0.2862]	[0.2724]	[0.2538]	[0.2298]	[0.1997]	[0.1622]	[0.1167]	[0.0626]	[0.0000]
6	[0.0000]	[0.0590]	[0.1131]	[0.1643]	[0.2133]	[0.2601]	[0.3040]	[0.3434]	[0.3789]
	[0.7797]	[0.7980]	[0.8101]	[0.8154]	[0.8132]	[0.8021]	[0.7807]	[0.7484]	[0.7056]
	[0.3165]	[0.2964]	[0.2731]	[0.2458]	[0.2133]	[0.1738]	[0.1259]	[0.0683]	[0.0000]
7	[0.0000]	[0.0652]	[0.1239]	[0.1788]	[0.2316]	[0.2830]	[0.3322]	[0.3784]	[0.4233]
	[0.7357]	[0.7576]	[0.7722]	[0.7785]	[0.7758]	[0.7625]	[0.7368]	[0.6981]	[0.6467]
	[0.3547]	[0.3280]	[0.2991]	[0.2675]	[0.2316]	[0.1891]	[0.1376]	[0.0753]	[0.0000]
8	[0.0000]	[0.0733]	[0.1383]	[0.1985]	[0.2563]	[0.3126]	[0.3671]	[0.4195]	[0.4735]
	[0.6916]	[0.7172]	[0.7342]	[0.7416]	[0.7384]	[0.7229]	[0.6929]	[0.6478]	[0.5879]
	[0.4016]	[0.3685]	[0.3339]	[0.2970]	[0.2563]	[0.2089]	[0.1520]	[0.0834]	[0.0000]
9	[0.0000]	[0.0834]	[0.1577]	[0.2261]	[0.2904]	[0.3513]	[0.4093]	[0.4663]	[0.5290]
	[0.6476]	[0.6767]	[0.6962]	[0.7047]	[0.7011]	[0.6833]	[0.6491]	[0.5974]	[0.5290]
	[0.4579]	[0.4195]	[0.3808]	[0.3384]	[0.2904]	[0.2348]	[0.1695]	[0.0927]	[0.0000]

The thickness of the obtained shell structure is varied to achieve different relative densities $\bar{\rho}$,

$$\bar{\rho} = \frac{\Omega_s}{\Omega_{tot}} \quad (4)$$

with Ω_s denoting the volume of the shell structure contained within the volume Ω_{tot} of the fundamental FCC tetrahedron.

3. Computational models

In order to gain insight into the mechanical behavior of shell-lattice materials over a wide range of relative densities, finite element simulations are conducted on unit-cells using the non-linear finite element software Abaqus/Standard. The same procedure is applied to the widely-used octet truss-lattice metamaterial for both comparison and validation purposes.

3.1. Constituent material

A simple J2-plasticity model with isotropic hardening is chosen for the constituent material. We choose a Young's modulus of $E = 200$ GPa, a Poisson's ratio of $\nu = 0.3$, and a Swift hardening law

$$k_s[\bar{\varepsilon}_p] = A(\bar{\varepsilon}_p + \varepsilon_0)^n \quad (5)$$

with the Swift parameters $A = 842.5$ MPa, $\varepsilon_0 = 0.036$ and $n = 0.176$. These values are chosen based on manufacturer provided data (yield strength, ultimate strength and ductility) for the additively-manufactured 316L stainless steel (CL20ES powder, Concept Laser) used for experiments.

3.2. Unit-cell meshes and periodic boundary conditions

Cubic unit-cells are considered due to the simplicity of boundary condition implementation they offer. The meshes are generated directly in Matlab, based on the 2D mesh within the fundamental tetrahedron. Solid elements are created by thickening the smooth shell structure along the local surface normal directions. The total volume of the mesh is estimated and compared to that of the tetrahedron, and the Newton-Raphson method is applied to find the appropriate thickness for the desired relative density.

Table 2

Wall thickness of TPMS-like shell-lattice as function of the relative density for a unit-cell side length of 1.

Density	0.01	0.02	0.05	0.1	0.2	0.3	0.4	0.5	0.6
Thickness	$2.09 \cdot 10^{-3}$	$4.18 \cdot 10^{-3}$	$1.05 \cdot 10^{-2}$	$2.09 \cdot 10^{-2}$	$4.21 \cdot 10^{-2}$	$6.39 \cdot 10^{-2}$	$8.64 \cdot 10^{-2}$	$1.10 \cdot 10^{-1}$	$1.36 \cdot 10^{-1}$

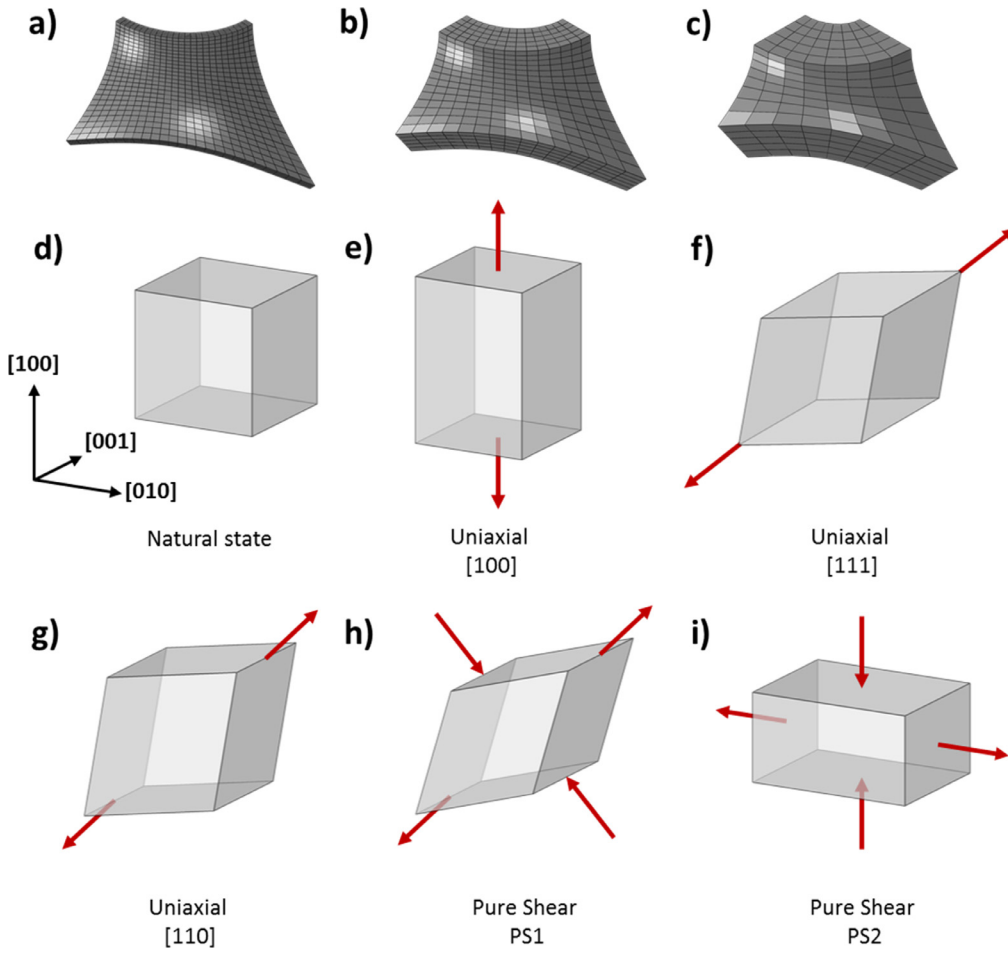


Fig. 5. a-c) 3D mesh contents of the fundamental tetrahedron for $\beta = 1$. a) 25×25 grid, $\bar{\rho} = 0.05$ b) 15×15 grid, $\bar{\rho} = 0.2$ c) 8×8 grid, $\bar{\rho} = 0.4$. d-i) Loading scenarios corresponding to the extrema of the stiffness and yield strength in uniaxial tension and pure shear. d) reference configuration, e) uniaxial tension/compression loading along the [100] direction, f) uniaxial tension/compression loading along the [111] direction, g) uniaxial tension/compression loading along the [110] direction, h) pure shear loading (PS1) with principal stress directions along the [110] and [110] axes, i) pure shear loading (PS2) with principal stress directions along the [100] and [010] axes.

Once the appropriate thickness is determined for a given relative density (Table 2), the 2D mesh is copied, mirrored and translated to produce a shell mesh filling the unit-cell. Using the same method as above to convert from 2D to 3D elements, five elements through thickness are used in all meshes. The number of 2D elements used in the tetrahedron varies with the target relative density. A grid of 25×25 elements is used for relative densities of 0.01, 0.02 and 0.05 (Fig. 5a), 15×15 elements for relative densities of 0.1 and 0.2 (Fig. 5b), and 8×8 elements for relative densities of 0.3, 0.4, 0.5 and 0.6 (Fig. 5c). C3D8I elements are used in simulations. Given the slenderness of the lightest shell structures and the resulting high element aspect ratios, the elastic results are compared to those obtained with a mesh featuring 50×50 elements (2,400,000 elements in the unit-cell). The mean elastic properties with both discretizations are within 1% of each other. Meshes of the octet-truss lattice unit-cell are similarly deduced from automatic meshes of the tetrahedron contents.

Kinematic constraints are imposed on the matching nodes of each pair of parallel unit-cell boundary surfaces, with the difference in displacement equal to the displacement of a dummy node. As a result, homogenized strains can be controlled, while node-wise displacement differences to the dummy node are possible, granted they follow the periodicity of the lattice. Three dummy nodes are introduced. Given a unit-cell side length of 1, their 9 degrees of freedom corresponding to the components of the displacement gradient \mathbf{H} , while the forces applied onto them correspond to the components of the Piola

stress tensor \mathbf{P} . Linear constraints between the dummy nodes are used to enforce symmetry of those tensors and thus reduce the number of degrees of freedom to the strict necessary of six; under those conditions, \mathbf{H} is equal to the small strain tensor $\boldsymbol{\varepsilon}$. An additional layer of dummy nodes is used to control the orientation of loading.

3.3. Elastic small-strain simulations

Elastic simulations are performed to determine both the homogenized elastic response, and the local stress field. The basis material is modeled as purely elastic without any plasticity. For both the shell- and truss-lattice unit-cells, six simulations are performed. In each simulation, one component of the small strain tensor is set to reach a value of 10^{-4} , while the other components are kept equal to 0. Those simulations are performed for relative unit-cell densities of 0.01, 0.02, 0.05, 0.1, 0.2, 0.3, 0.4, 0.5 and 0.6.

From these simulations, all components of the macroscopic elastic stiffness matrix \mathbf{A}_{tot} are readily obtained from the computed macroscopic stress-strain response. In addition, the stress response is recorded at integration points of each element n . This linear localization relationship, i.e. the relation between the local stress tensor σ_n and the applied macroscopic strain tensor, is described by the matrices \mathbf{A}_n . The local stress response can then also be related to the applied stress \mathbf{P} at the macroscopic level,

$$\sigma_n = \mathbf{A}_n \mathbf{A}_{\text{tot}}^{-1} \mathbf{P} \quad (6)$$

We note that the macroscopic Piola stress is equal to the macroscopic Cauchy stress for small strains.

We make use of (6) to estimate the macroscopic yield stress. To obtain a high resolution pole figures of the macroscopic yield stress of FCC metamaterials, a correspondingly high number of directions $\mathbf{a}^{(i)}$ needs to be considered. With the availability of (6), we can then compute the local stress field for any arbitrary macroscopic stress tensor \mathbf{P} without running additional elasto-plastic finite element simulations. Based on the elastic solution of the unit-cell problem, the macroscopic yield stress for a direction $\mathbf{a}^{(i)}$ is then defined as the minimal value of $|P^{(i)}|$ for which the local von Mises equivalent stresses $\bar{\sigma}_n$ due to the macroscopic loading by the stress tensor $\mathbf{P}^{(i)} = P^{(i)} \mathbf{a}^{(i)} \otimes \mathbf{a}^{(i)}$ exceeds the basis material yield strength within 5% of the volume of the solid phase. The pole figures shown in the present paper have all been generated based on data for about 21,000 directions of loading.

3.4. Elastoplastic finite-strain simulations

Large strain simulations assuming an elasto-plastic material behavior are performed on all unit-cell models (covering relative densities of 0.1, 0.2, 0.3, 0.4, 0.5 and 0.6). Three basic loading scenarios are considered: uniaxial tension, uniaxial compression and pure shear, to be understood in the sense of the Piola stress \mathbf{P} (engineering stress). Introducing a scalar parameter λ that evolves from 0 to λ_{\max} during the simulations, the loading conditions may be written in terms of the components of the macroscopic displacement gradient \mathbf{H} and the stress tensor \mathbf{P} in the coordinate frame $\{\mathbf{e}_1, \mathbf{e}_2, \mathbf{e}_3\}$:

- Uniaxial tension:

$$\begin{cases} H_{11} = \lambda \\ P_{12} = P_{13} = P_{23} = P_{22} = P_{33} = 0 \end{cases} \quad (7)$$

- Uniaxial compression:

$$\begin{cases} H_{11} = -\lambda \\ P_{12} = P_{13} = P_{23} = P_{22} = P_{33} = 0 \end{cases} \quad (8)$$

- Pure shear:

$$\begin{cases} H_{12} = H_{21} = \lambda \\ P_{11} = P_{13} = P_{23} = P_{22} = P_{33} = 0 \end{cases} \quad (9)$$

Uniaxial tension and compression simulations are performed for three different unit-cell orientations, i.e. with the \mathbf{e}_1 -direction being parallel to the [100], [110] and [111] directions. Pure shear simulations are performed in the unit-cell's natural coordinate frame (case PS1), as well as with a rotation of 45 degrees around the 3rd coordinate axis (case PS2). All loading scenarios are illustrated in Fig. 5.

To evaluate and compare the specific energy absorption capability of metamaterials, the plastic dissipation is computed up to the same applied macroscopic strain. In particular, we chose the loading parameter λ such that a von Mises material would exhibit the same energy dissipation for all loading cases, with a final equivalent plastic strain of $\bar{\epsilon}^p = 0.36$. This lead to maximal values of λ of 0.3 in uniaxial compression, 0.43 in uniaxial tension and 0.32 in pure shear.

The specific energy absorption ψ is then defined as the total plastic dissipation per unit mass,

$$\psi = \frac{D}{\rho} \quad (10)$$

with D denoting the plastic dissipation density, and ρ denoting the mass density.

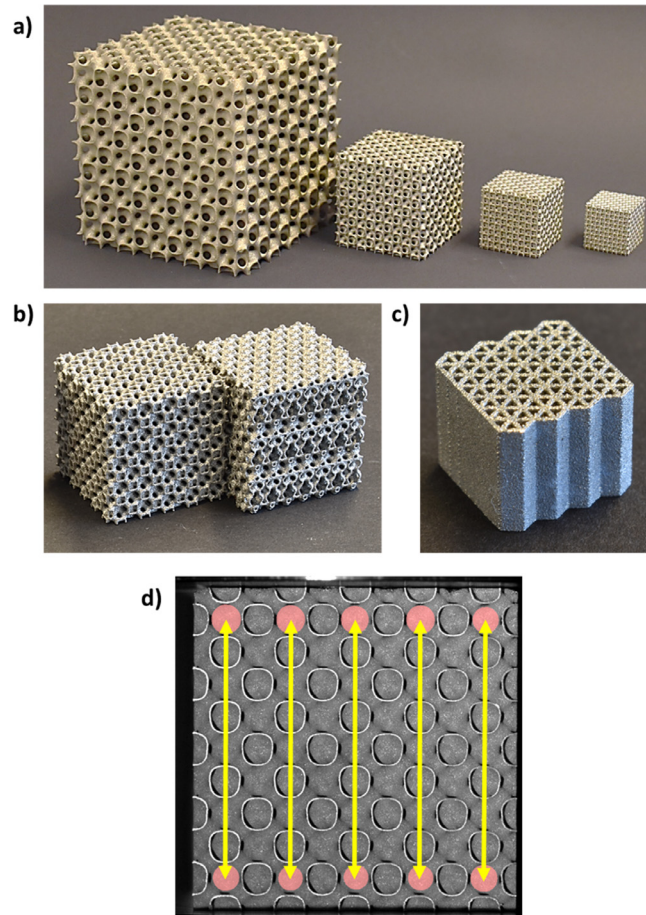


Fig. 6. a) View of untested uniaxial compression specimens produced via selective laser melting using a 316 L stainless steel powder. Each specimen consists of $5 \times 5 \times 5$ unit-cells with $40 \mu\text{m}$ wall thickness, with relative densities from left to right: 0.1, 0.2, 0.3 and 0.4. b) View of untested (left) [100]-oriented specimen and (right) [111]-oriented specimen of $\beta = 0.375$ iso-shell-structure of relative density $\bar{\rho} = 0.3$. c) View of triangular honeycomb specimen of relative density $\bar{\rho} = 0.67$. d) Position of virtual extensometers used to determine compressive strains via digital image correlation.

4. Experimental procedures

The main purpose of the experiments is to validate the computational results. Given the high level of confidence in the reliability of non-linear finite element analysis, only a small subset of the computational results is reproduced experimentally.

4.1. Specimens

All specimens have been manufactured using a selective laser melting system (Model M2, Concept Laser) with CL 20ES powder (Concept Laser) with a stainless steel 316L particle size distribution in the range $20\text{--}50 \mu\text{m}$.

4.1.1. First batch of shell-lattice specimens to validate the relative density scaling for $\beta = 1$

In order to confirm the numerically-estimated scaling of large-deformation properties of the shell-lattices, uniaxial compression experiments are performed on $\beta = 1$ specimens oriented in the [100] direction, for relative densities of 0.1, 0.2, 0.3 and 0.4. The specimens are tested along the building direction. Cubic specimens consisting each of $5 \times 5 \times 5$ unit-cells are produced. In an attempt to minimize variations of the basis material properties related to the manufacturing process, the same wall thickness of $400 \mu\text{m}$ is chosen for all specimens. This leads to cube edge lengths of 95.6 mm, 47.5 mm, 31.4 mm, and 23.2 mm, respectively. Fig. 6a shows a photograph of the manufactured specimens. The external overall dimensions of the produced specimens are found to be within 1% of the prescribed ones. The measured masses of the specimens are within 2% of the prescribed ones assuming a basis material density of $\rho_b = 8 \text{ g/mm}^3$.

4.1.2. Second batch of shell-lattice specimens to validate reduced plastic anisotropy for elastically-isotropic shell-lattices

To confirm and compare the numerically-observed plastic anisotropy of shell-lattices, uniaxial compression experiments are conducted on specimens of relative density 0.3 for $\beta = 1$ (TPMS-like) and $\beta = 0.375$ (iso-shell). For each structure, the experiments are conducted on specimens oriented in the [100] and in the [111] directions. The [100] specimens consist in cubic blocks of $5 \times 5 \times 5$ unit-cells, while the [111] specimens included $4.95 \times 5.2 \times 4.90$ unit-cells. For a wall thickness of $400 \mu\text{m}$, the TPMS-like and iso-shell specimens feature an edge length of about 31mm, and 29mm. To avoid the use of building supports, the [111]-oriented specimens are built with the tested direction transverse to the building direction. To allow for meaningful comparison, all specimens of this batch are therefore tested transversely to the building direction. Two repeats of each experiment are performed to confirm the repeatability of the response. Fig. 6b shows the manufactured [100] and [111] iso-shell specimens. The measured outer dimensions of the specimens are within 1% of the prescribed ones, while the weight measurements suggest relative densities ranging from 27% to 28%.

4.1.3. Honeycomb-like specimen to identify stress-strain curve of basis material

The hardening curve used for modeling purposes had been chosen based on basic data provided by the manufacturer (yield stress, strength and ductility). In order to gain insight into the stress-strain response of the as-manufactured cell wall material, uniaxial compression experiments are performed. Given that the material properties of additively manufactured materials usually depend on the wall thickness, a triangular honeycomb with the same wall thickness $t_w = 400 \mu\text{m}$ as that of the manufactured shell-lattice specimens is employed (instead of manufacturing cylindrical compression specimens). Note that despite the complex honeycomb geometry, the stress-state for compression between two flat loading platens is expected to be uniaxial tension in all cell walls. A relative density of 67% is selected to guarantee a high structural stability of the honeycomb specimen for compressive strains of up to 0.2. Preliminary simulations suggested that lower density specimens would respond by cell buckling at lower strains. The resulting honeycomb specimen (Fig. 6c) features a truss length of 1.64mm. The specimen comprises 13×8 triangles for total in-plane dimensions of 11.94 mm \times 11.76 mm, and measures 10mm in height.

For comparison purposes, we also extract standard tensile specimens from 1.5 mm thick, cold-wrought and annealed, stainless steel 316L sheets (AISI 316L Finish 2B, provided by Aperam, France). The tension experiments with optical strain measurements are performed on a universal testing machine at a strain rate of 10^{-3}s^{-1} .

4.2. Macroscopic compression experiments

The shell-lattice specimens are tested using a screw-driven universal testing machine (Model RME250, Zwick) equipped with two flat steel loading platens and a 250 kN load cell. No grease or lubricant is applied to the platens. For each specimen a crosshead velocity corresponding to a constant engineering strain rate of 2×10^{-3} is applied. A high-resolution digital camera (4240×2824 pixels, Model GS3-U3-120S6M-C, PointGrey) is installed to monitor one face of the specimen, with a resolution of about 500 pixels per unit-cell. Macroscopic engineering strains are estimated through digital image correlation using the software Vic-2D (Correlated Solutions). Five virtual extensometers are placed between the centers of the unit-cells of the top and bottom row (Fig. 6d). The reported engineering strain corresponds to the average of all five extensometers.

4.3. Microscopic analysis

Additional single-unit-cell specimens with $\beta = 1$, $\bar{\rho} = 0.3$, and $t_w = 400 \mu\text{m}$, are manufactured for microscopic analysis. The specimens are embedded in a conductive resin, grinded and polished. Electron Back-Scattered Diffraction (EBSD) analysis is performed with a step size of $0.5 \mu\text{m}$ in the central part of a cell wall's cross-section. A spare honeycomb specimen is polished and used to check for internal porosity and surface roughness.

5. Results

The results section is split into three main parts. The first set of results is concerned with the anisotropic mechanical properties of the TPMS-like shell-lattice ($\beta = 1$) and the octet truss-lattice. The second set of results then focuses on the properties of elastically-isotropic shell-lattices ("iso-shell"), before discussing the stress-strain response and microstructural features of the additively-manufactured stainless steel cell walls.

5.1. Results for the anisotropic shell- and truss-lattices

5.1.1. Scaling of the elastic properties

Both the shell- and truss-lattice structures feature cubic symmetry. As a consequence, their stiffness matrix is fully defined through three distinct elastic constants. For a Cartesian coordinate system aligned with the (100) set of directions,

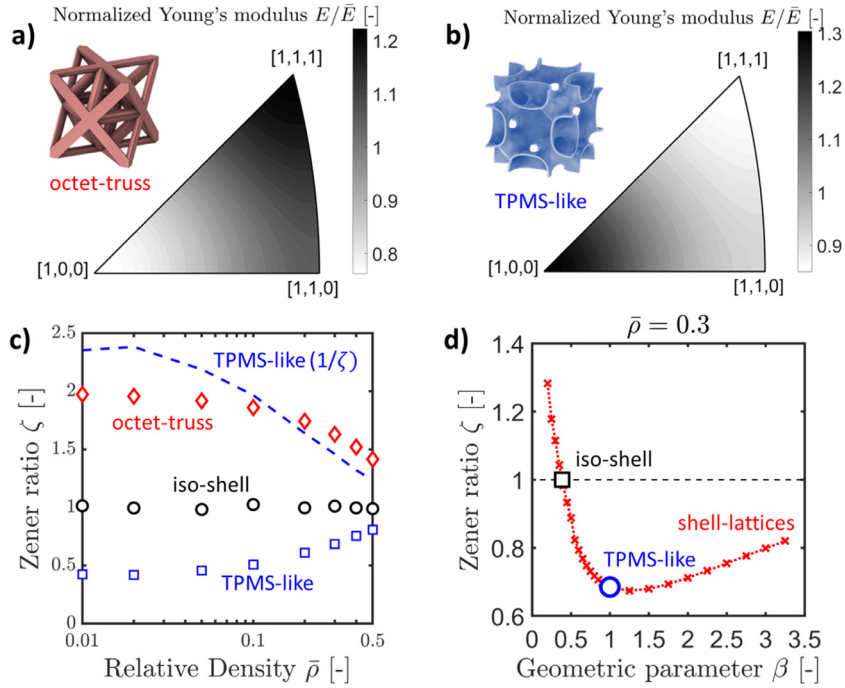


Fig. 7. Elastic anisotropy: pole figures of the Young's moduli (as normalized by the mean for all directions) at relative density $\bar{\rho} = 0.2$ for (a) the octet-truss, and (b) the TPMS-like structure (i.e. $\beta = 1$). (c) Zener anisotropy ratio as a function of the relative density. (d) Zener anisotropy ratio as a function of the geometric parameter β for relative density $\bar{\rho} = 0.3$.

$$C = \begin{bmatrix} C_1 & C_2 & C_2 & 0 & 0 & 0 \\ C_2 & C_1 & C_2 & 0 & 0 & 0 \\ C_2 & C_2 & C_1 & 0 & 0 & 0 \\ 0 & 0 & 0 & C_3 & 0 & 0 \\ 0 & 0 & 0 & 0 & C_3 & 0 \\ 0 & 0 & 0 & 0 & 0 & C_3 \end{bmatrix} \quad (11)$$

with the three elastic constants C_1 , C_2 and C_3 . Note that commonly-used elastic constants such as the Young's modulus E and the shear modulus G depend on the orientation of the loading direction with respect to the cubic unit-cell.

This direction-dependency for the anisotropic shell-lattice and the octet truss-lattice are shown in Fig. 7, which includes pole figures of the Young's modulus for both metamaterials at a relative density of 0.2. It becomes immediately apparent from Fig. 7a that the octet truss-lattice is stiffest when loaded along the [111] direction, and softest when solicited along the [100] direction. The opposite trend is observed for the TPMS-like shell-lattice (Fig. 7b) despite the fact that it features the same FCC symmetries as the octet truss. A similar qualitative difference is observed with regards to shear loading: the octet truss shows the highest shear modulus in the PS1 configuration and its lowest in the PS2 configuration, while the opposite order is observed for the shell-lattice.

The degree of elastic anisotropy of cubic metamaterials can be conveniently measured by Zener's anisotropy ratio

$$\zeta = \frac{2C_3}{C_1 - C_2} = G_1/G_2, \quad (12)$$

which corresponds to the ratio of the shear moduli for the loading cases PS1 and PS2. The scaling of the Zener anisotropy ratio with relative density is presented in Fig. 7c. For the octet truss, it decreases from a value of 2 at very low relative densities to 1.4 for a relative density of 0.6. A similar trend is observed for the TPMS-like shell-lattice, i.e. the anisotropy decreases as the relative density increases. The ratio of the maximum to minimum shear modulus is 2.4 at low density, i.e. the TPMS-like structure exhibits a slightly higher anisotropy than the octet truss at low relative densities. However, the two curves intersect at relative density of about 0.15. In other words, the shell-lattices are less anisotropic than the truss-lattices at relative densities above 0.15.

The scaling of the elastic moduli, i.e. their evolution as a function of the relative density, is shown in Fig. 8. To highlight the scaling and to ensure a good readability of our plots, the computed macroscopic moduli are normalized by the Voigt bounds (basis material modulus times the relative density). To allow for meaningful comparisons of the stiffness of the anisotropic metamaterials, the maximum, minimum, and average values of the Young's and shear moduli are reported

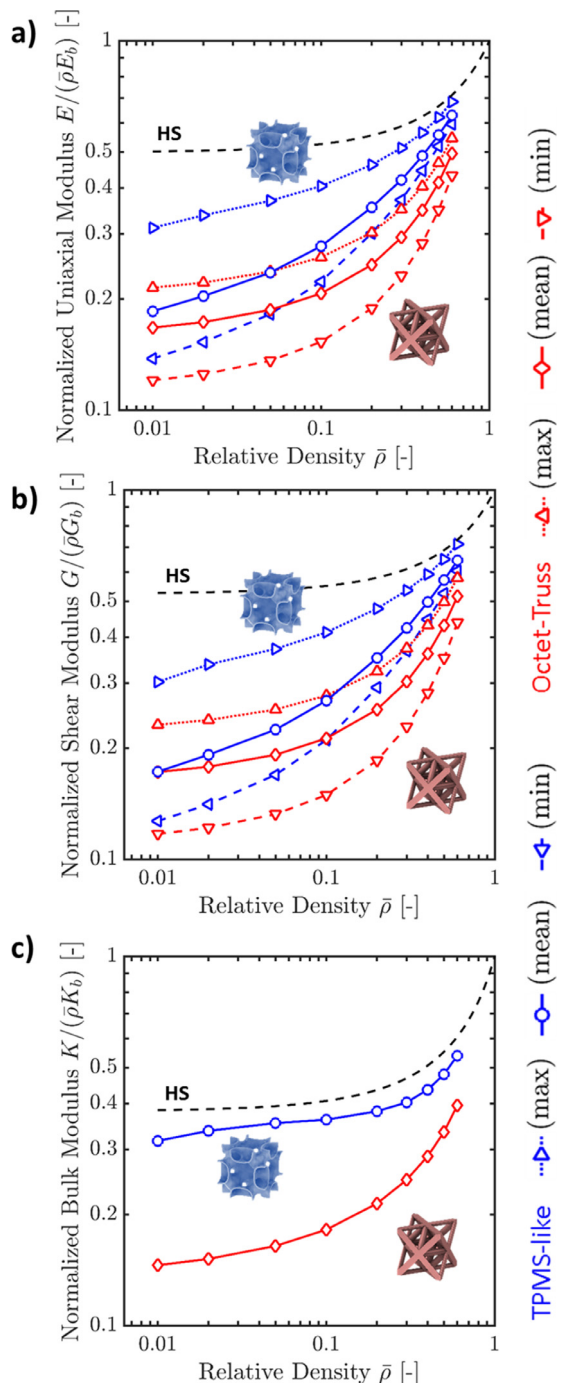


Fig. 8. Compared scaling of elastic moduli with relative density for the octet-truss and the proposed smooth curvature structure: (a) Tensile modulus, (b) shear modulus, (c) bulk modulus. Dashed lines represent the Hashin-Shtrikman (HS) bounds for isotropic porous structures.

for each relative density. It transpires from the results that the shell-lattices exhibit high specific stiffness at high relative densities; it approaches the Hashin-Shrikman (HS) bounds ([Hashin and Shrikman, 1963](#)) much faster than the stiffness of the octet trusses. At low relative densities, the mean stiffness of the TPMS-like shell-lattice is still slightly higher than that of the octet trusses of equal mass, but it is far from the HS bounds. Moreover, while the octet truss response enters the sub-optimal, but linear scaling regime at low densities (e.g. the theoretical E-Modulus scaling factor is 1/5 when the octet truss is loaded along the [111] direction), the scale factor of the shell-lattices continues to decrease as the relative density decreases.

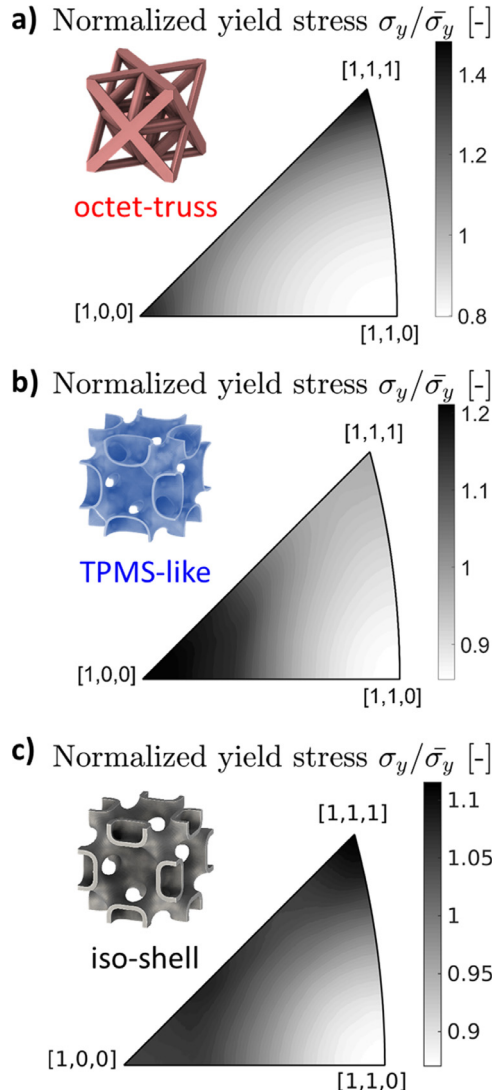


Fig. 9. Anisotropic yield under uniaxial loading (normalized by the mean for all directions): (a) pole figure of normalized yield stress of the octet-truss at relative density $\bar{\rho} = 0.01$, (b) pole figure of normalized yield stress of the TPMS-like shell-lattice at relative density $\bar{\rho} = 0.01$, (c) pole figure of normalized yield stress of the isotropic shell-lattice at relative density $\bar{\rho} = 0.01$.

For all relative densities considered, the shear modulus of the TPMS-like shell-lattices is also higher than that of the octet trusses (Fig. 8b). The highest mean shear stiffness advantage of more than 40% is observed at relative densities of 0.2 to 0.3. The maximum longitudinal and shear stiffness of the shell-lattices is always higher than the highest stiffness of the octet trusses of the same relative density. The same is observed for the lower bounds: the softest direction of the TPMS-like shell-lattice is always stiffer than the softest direction of the octet truss for the same relative density. The differences are even more pronounced for the bulk moduli (Fig. 8c), where the shell-lattice is more than twice as stiff as the octet truss at low relative densities. The bulk modulus of the shell-lattice is actually close to the theoretical HS limit (dashed line) for porous solids.

The above stiffness estimates are partially validated by comparing the computational results for the octet-truss lattice at $\bar{\rho} = 0.01$ with the analytical results by Deshpande et al. (2001b), which apply in the limit of infinitesimal relative densities. It is found that the numerical modulus estimates are close to the analytical values (maximum difference of less than 8%).

5.1.2. Scaling of the initial yield stress

Fig. 9 shows the direction dependency of the yield stress for uniaxial tension of structures of relative density 0.01 (results for other relative densities are qualitatively similar, while less anisotropic). The results depicted in Fig. 9a show that the octet truss exhibits only 80% of the average yield stress when solicited in the [110] direction, while pronounced yield strength

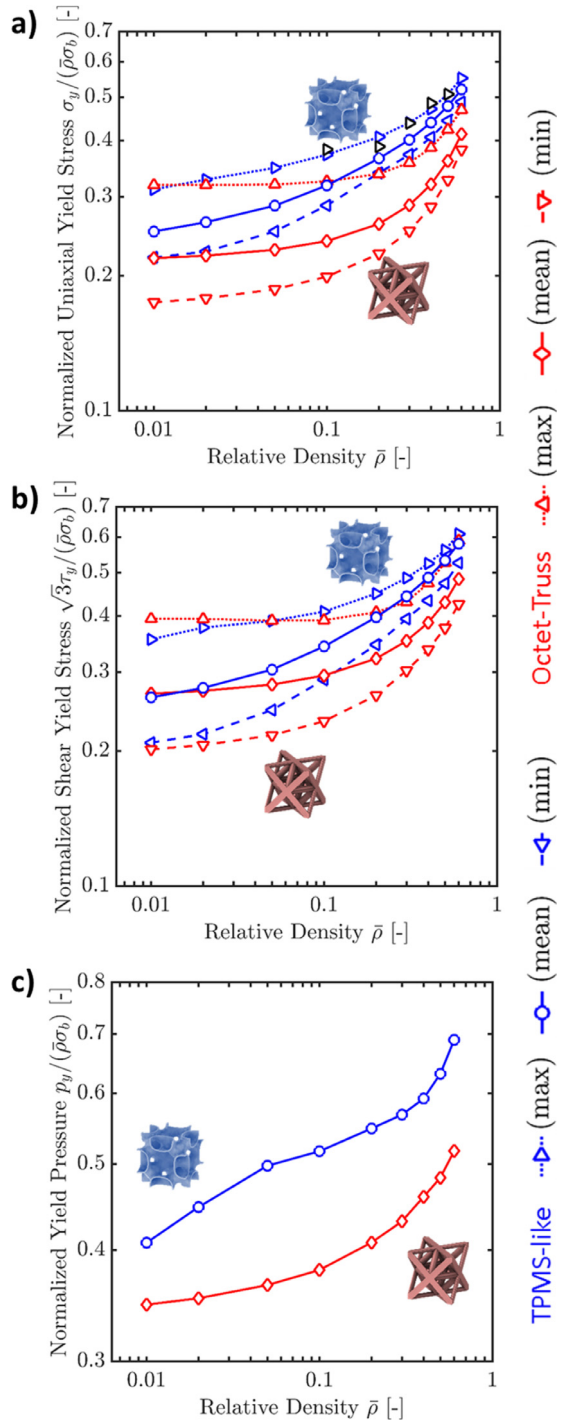


Fig. 10. Maximum, minimum and average yield properties under (a) uniaxial tension/compression, (b) pure shear, (c) hydrostatic tension/compression as deduced from field elastic response. Black dots represent experimental results.

peaks ($\approx 145\%$ of the mean) are observed for loading along the [111] and [100] directions (the stiffer and softest directions, respectively, see Fig. 7a). The TPMS-like shell-lattice (Fig. 9b) displays a less pronounced yield strength peak (about 120% of mean) in the [100] direction (that of highest stiffness), while the [110] direction is the weakest with only 88% of the mean yield strength. The yield strength of the shell-lattice for the [111] direction is close to the mean.

Fig. 10 provides an overview on the scaling of yield properties for both metamaterials in a variety of scenarios. Properties are normalized using the relative density $\bar{\rho}$ and the bulk-material yield stress σ_b . Similar to the elastic properties, the yield

strength of the TPMS-like shell-lattice is higher than that of the octet truss in almost all cases investigated. Fig. 10a presents the scaling of yield stresses under uniaxial loading with relative density. As already indicated by the pole figures (Fig. 9), the directional spread of yield values is more pronounced for the octet truss than for the shell-lattice: for the octet truss, the maximum to minimum value ratio is 1.23 for $\bar{\rho} = 0.6$, and 1.83 for $\bar{\rho} = 0.01$, to be compared with 1.13 and 1.42 for the anisotropic shell-lattice at the same relative densities. Overall the shell-lattice shows higher yield values than the octet truss. Taking the ratio of mean values for yield stress, we find 1.26 for $\bar{\rho} = 0.6$ and 1.15 for $\bar{\rho} = 0.01$.

Fig. 10b shows the scaling of maximum, mean and minimum yield properties under pure shear loading with relative density. The smooth structure is consistently stronger in these conditions for relative densities above 0.1; for example, its mean value is 1.20 times that of the octet truss for $\bar{\rho} = 0.6$, while its poorer scaling leads to a value of 0.98 that of the octet-truss for $\bar{\rho} = 0.01$. Finally, Fig. 10c presents the scaling of yield stress with relative density under hydrostatic pressure. In this case, the TPMS-like shell-lattice is always stronger than the octet-truss lattice: 33% stronger for $\bar{\rho} = 0.6$, and 17% stronger for $\bar{\rho} = 0.01$.

The above results are partially validated by comparing numerical estimates for the octet truss (at the lowest investigated relative density of $\bar{\rho} = 0.01$) to the analytical pin-jointed truss model proposed by Mohr (2005). Comparing maximum, average and minimum yield strengths under uniaxial, pure shear and hydrostatic loading, the numerical and analytical values are in agreement with a maximum relative difference of 5%.

5.1.3. Large strain response

Fig. 11 presents the macroscopic engineering stress-strain curves obtained from elastoplastic simulations, for three scenarios (with different orientations) and the three relative densities (0.3, 0.2, 0.1) at which the metamaterials start exhibiting unstable behavior. Stability is understood here in the non-conservative sense of sustained hardening in a given loading scenario. When unit-cell simulations display a peak in the macroscopic stress, localization bands are expected to form in structures containing multiple unit cells. While the elastic and elastic limit properties presented above are fairly general (for an isotropic elasto-plastic basis material with J2 yield criterion), the large strain response is not. In particular, the stability of metamaterials is expected to depend on both the geometry of structure, and on the hardening behavior of the basis material. It is safe to assume that for a basis material with lower hardening modulus the two metamaterials considered herein would present a transition from stable to unstable behavior at higher relative densities.

The simulation results (Fig. 11) show that the TPMS-like shell-lattice is stronger and more stable than the octet truss, and confirm the loading direction dependency of the initial yield stress. For the shell-lattice, the hardening rates rank in the same order as the yield stresses. The [100] direction displays the highest hardening rate and appears stable at densities of 0.3 and 0.2, but unstable at 0.1. The weakest [111] direction is still stable with positive but very low hardening up to a compressive strain of 30% at a relative density of 0.3, and expectedly displays unstable behavior for lower relative densities. The same is true of the slightly-higher hardening [110] direction, which loses stability at a relative density of about 0.2. The initially stronger [111] and [100] directions of the octet truss show qualitatively similar (but quantitatively weaker) behaviors, with the former displaying unstable behavior starting at a relative density of 0.2, and the latter at 0.3. In all of these cases, as relative density diminishes the stress-strain curve gradually displays less hardening, until stability is lost. A remarkable exception to that rule is the stress-strain curve obtained when loading the octet truss along the [110] direction: some struts are then perfectly aligned with the loading direction, leading to a behavior that is up to a factor that of the bulk material, with important increase in force, as seen for relative densities of 0.3 and 0.2. Although this direction displays the lowest yield point, it has the highest hardening rate for the octet truss at those relative densities. The transition to unstable behavior (as seen for $\bar{\rho} = 0.1$) is sudden, as it is triggered by buckling at the strut level.

The advantages of the TPMS-like shell-lattice become even more pronounced for uniaxial tension (Fig. 11d-f). All engineering stress-strain curves for the shell-lattice exhibit a monotonically increasing response well past the basis material's maximum elongation (15% strain), and, up to a multiplicative factor, the response at different relative densities remains notably unchanged. A similar qualitative response is also observed when loading the octet truss along the [100] direction, but at a significantly lower stress level. For the two other loading directions, the tensile response exhibits an engineering stress peak at a strain of about 0.15, which corresponds to the peak force for the base material, associated with necking at the strut level, with the [110] direction lying at much lower stress levels (about 25% less at $\bar{\rho} = 0.3$ and 40% less at $\bar{\rho} = 0.4$ than the [111] direction, and both of them well below the stress-levels shown by the shell-lattice).

The shear stress-strain responses are depicted in Figs. 11g-i. The shell-lattice shows monotonically increasing stress for $\bar{\rho} \geq 0.2$, with lower relative hardening and larger stress difference between the two directions as the relative density decreases. Its response stays well above that of the octet truss for any of the two orientations considered. At $\bar{\rho} = 0.1$ it exhibits unstable behavior as a peak stress is reached around 10% strain. The octet truss displays an unstable response in its strongest orientation (PS1) at all relative densities shown (and already at $\bar{\rho} = 0.4$). The weaker orientation (PS2) is stable at $\bar{\rho} = 0.3$ and unstable at lower relative densities.

The blue macroscopic stress-strain curves shown in Fig. 11a, d, g are representative for the shell-lattice response at relative densities above $\bar{\rho} = 0.3$. Note that all curves increase monotonically, irrespective of the loading scenario. For $\bar{\rho} = 0.2$, the material response becomes instable in compression in the [110] and [111] directions, in the sense that the macroscopic stress-strain response for uniaxial compression exhibits a stress peak followed by a softening phase. And for $\bar{\rho} = 0.1$, all loading cases considered lead to an early ($< 30\%$ strain) peak force except for uniaxial tension. The comparison with the results for the octet truss (red curves in Fig. 11) reveal the higher stability of the large deformation response of the TPMS-

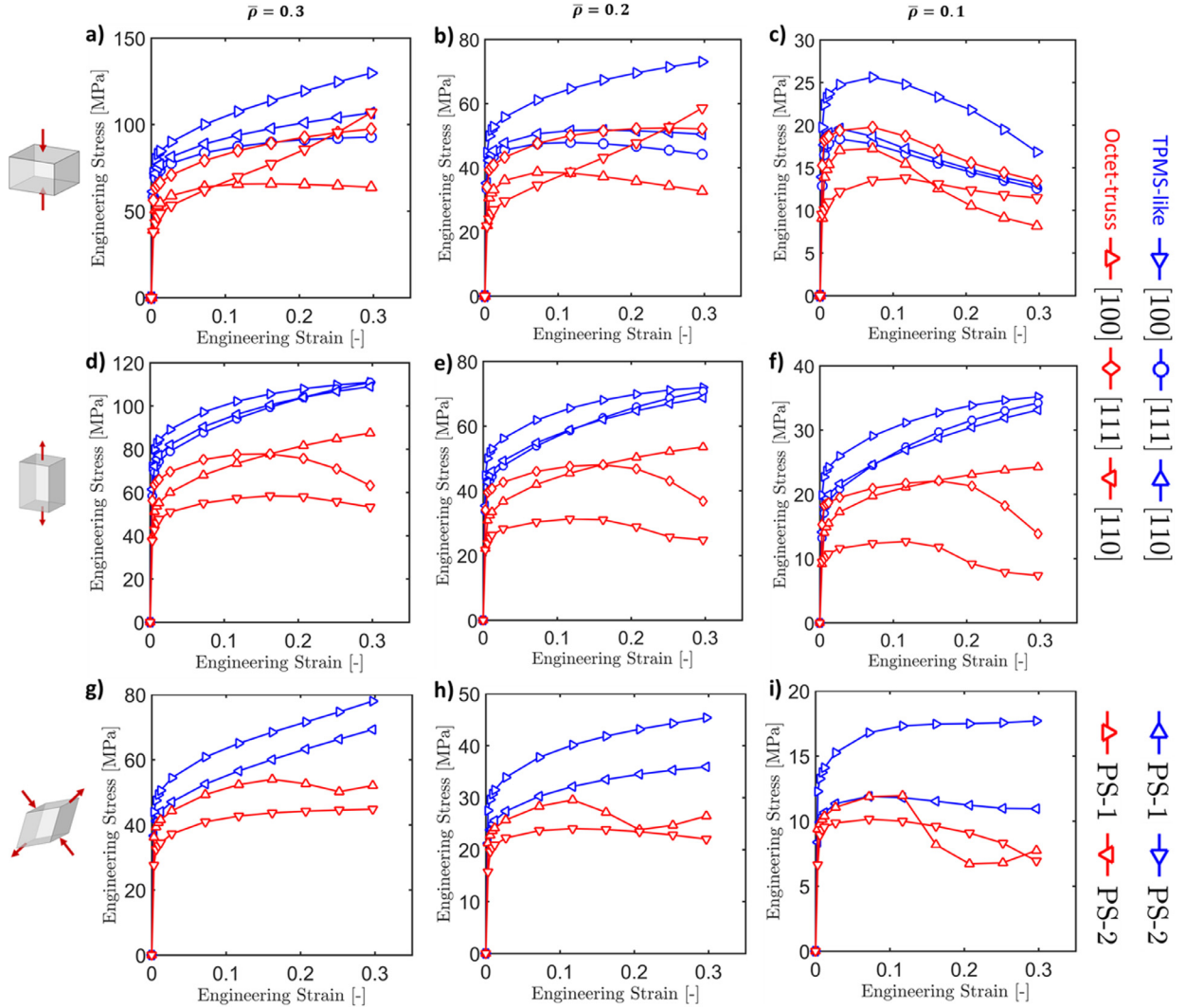


Fig. 11. Macroscopic engineering stress-strain curves of the TPMS-like shell-lattice and the octet-truss, for different loading scenarios: (a, b, c) uniaxial compression, (d-f) uniaxial tension, (g, h, i) pure shear; and different relative densities: (a, d, g) $\bar{\rho} = 0.3$, (b, e, h) $\bar{\rho} = 0.2$, and (c, f, i) $\bar{\rho} = 0.1$. (For interpretation of the references to color in this figure legend, the reader is referred to the web version of this article.)

like shell-lattice. For the octet truss architectures, all force-displacement curves exhibit stress peaks for $\bar{\rho} = 0.2$, and some already for $\bar{\rho} = 0.3$.

5.1.4. Scaling of the specific energy absorption

To evaluate the Specific Energy Absorption (SEA) capability of the proposed metamaterials, we computed the plastic dissipation from the simulations for different relative densities. In Fig. 12, the plastic dissipation per unit volume (as normalized by the plastic dissipation of the basis material times the relative density) is plotted as a function of the relative density. This measure is identical to the ratio of the specific energy absorption of the metamaterial and that of the basis material,

$$\frac{D}{D_b \bar{\rho}} = \frac{D \rho_b}{D_b \rho} = \frac{\psi}{\psi_b} \quad (13)$$

where the subscript b indicates values for the bulk material. For uniaxial compression (Fig. 12a), it can be seen that the SEA of the TPMS-like shell-lattice is almost always higher than that of the octet truss – irrespective of the loading direction and relative density. The SEA for the weakest direction of the shell-lattice structure is approximately equal to the SEA for the strongest direction of the SOT structure. It is worth noting that the overall structural efficiency increases as the relative density increases. For a relative density of $\bar{\rho} = 0.5$, we have $D_{TPMS} \cong 0.55 \bar{\rho} D_b$, while it is only about $0.2 \bar{\rho} D_b$ at a relative density of $\bar{\rho} = 0.1$. Moreover it is expected that for configurations that show a local peak in force, the overall response of

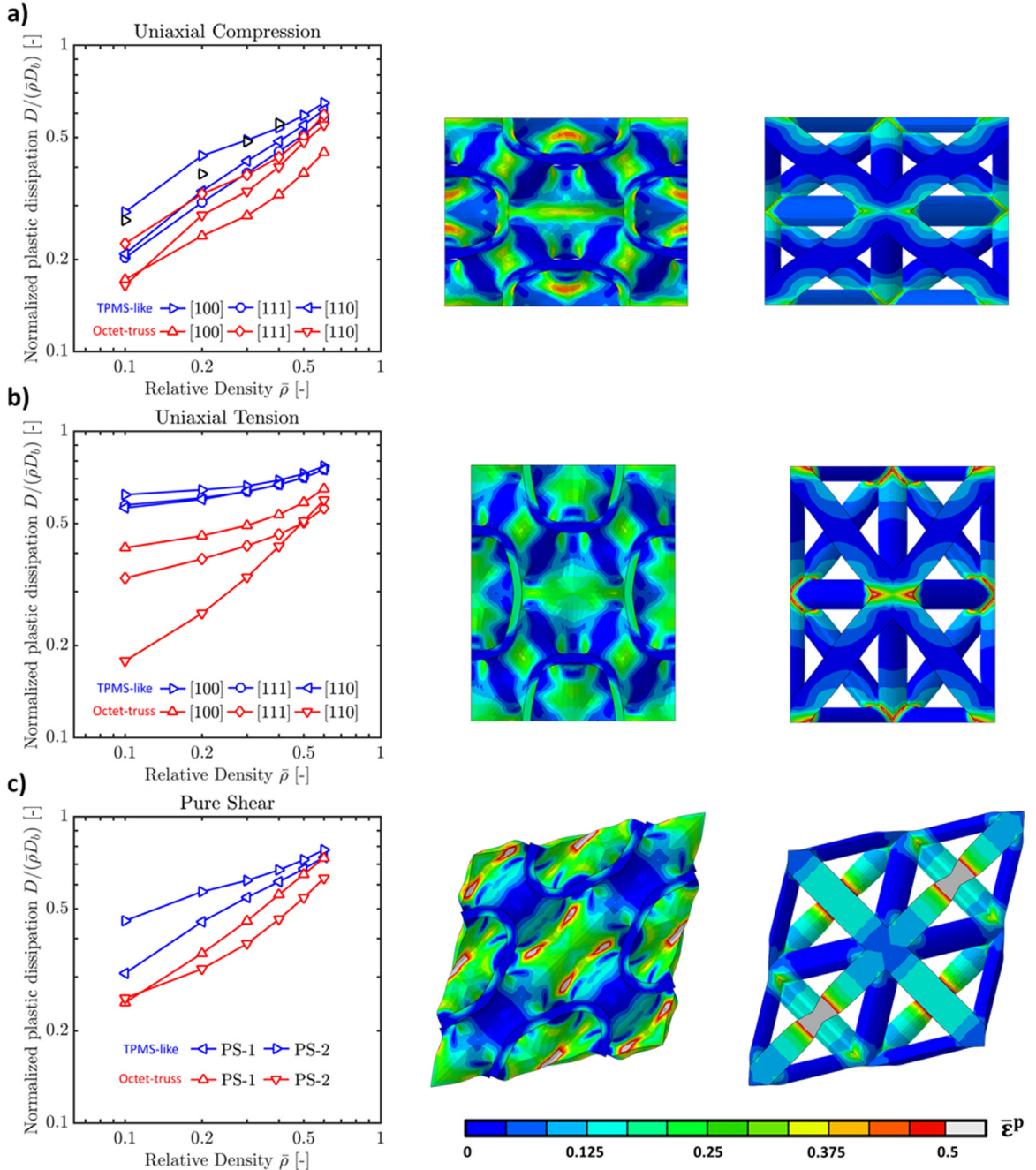


Fig. 12. Compared scaling of normalized plastic dissipation of the octet-truss and the TPMS-like shell-lattice for different loading scenarios and orientations, and associated deformation with color-coded equivalent plastic strain at 18% engineering strain. (a) uniaxial compression, pattern in compression along [100] (b) uniaxial tension, pattern in tension along [100] (c) pure shear, deformation pattern under loading PS1. Black open symbols in (a) represent experimental results. (For interpretation of the references to color in this figure legend, the reader is referred to the web version of this article.)

larger scale structures comprising several unit-cells would differ slightly: localization bands, shear bands, and a resulting plateau in force that would impact the SEA of the structure.

In the case of uniaxial tension (Fig. 12b), the energy absorbed by the shell-lattice is significantly higher than that of the octet truss for all directions of loading. Moreover, the scaling is more stable (nearly linear) for uniaxial tension than for uniaxial compression. It should be noted that the comparison point is beyond the maximum force of the bulk material: the bulk dissipation value assumes uniform strain and would be an overestimate in the case of an actual component loaded in tension, where the necking and fracture are likely to limit the energy absorption capability. The same is true of un-stable

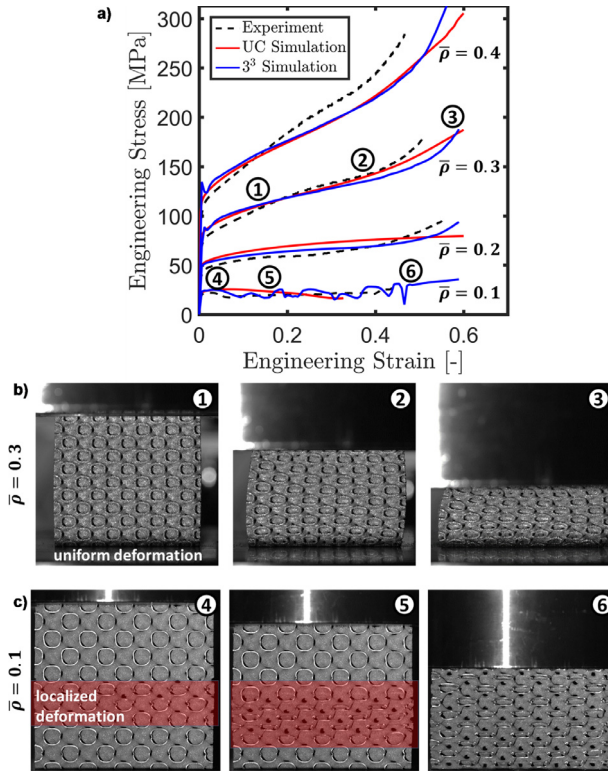


Fig. 13. Results from uniaxial compression experiments of the TPMS-like shell-lattice (i.e. $\beta = 1$) along the [100] direction: a) experimental and computational stress-strain curves. b) selected photographs of the deformed specimen for $\bar{\rho} = 0.3$ c) selected photographs of the deforming specimen for $\bar{\rho} = 0.1$. (For interpretation of the references to color in this figure legend, the reader is referred to the web version of this article.)

directions for the metamaterials (here, for the octet truss only). At a relative density of $\bar{\rho} = 0.5$, we have $D_{TPMS}^{UT} \cong 0.75\bar{\rho}D_b$, which drops only slightly to $D_{TPMS}^{UT} \cong 0.6\bar{\rho}D_b$ at $\bar{\rho} = 0.1$. As for uniaxial compression, the specific energy absorption under uniaxial tension is the highest for loading along the [100] direction of the shell-lattice structure. The octet truss has widely different energy absorption depending on the loading direction, due to localization within the struts depending on their alignment with the loading direction, and in any case much lower absorption capability in tension.

At a relative density of $\bar{\rho} = 0.5$, the scaling of the energy absorption capability of the shell-lattice for shear (Fig. 12c) is comparable to that for uniaxial tension, i.e. $D_{TPMS}^{PS} \cong 0.7\bar{\rho}D_b$. However, it decreases to $D_{TPMS}^{PS} \cong 0.45\bar{\rho}D_b$ for loading a TPMS-like shell-lattice of $\bar{\rho} = 0.1$ in the PS2 case. In any case, it is always higher than that of the octet truss, in particular at low relative densities.

5.1.5. Experimental validation

Fig. 13a shows the measured engineering stress-strain curves for uniaxial compression along the [100] direction of the additively-manufactured TPMS-like shell-lattice specimens. The experimental results for $\bar{\rho} = 0.3$ and $\bar{\rho} = 0.4$ are in reasonable agreement with the unit-cell simulations. For strains between 5% and 30%, the experimentally-measured and numerically-predicted stresses are within 10% of each other. The simulation for $\bar{\rho} = 0.2$ consistently overestimates the stress by 15% over that range, which is attributed to a larger sensitivity to imperfect boundary conditions. Switching from unit-cell models with periodic boundary conditions to models of cubic specimens composed of $3 \times 3 \times 3$ unit cells (blue curves in Fig. 13a) reduces the maximum difference in stress to less than 9%. The overall stress level for $\bar{\rho} = 0.1$ is also similar for the experiment and the simulation, but the specimen size-dependent oscillation of the stress-strain curve is not captured by the unit-cell simulation (as expected). Photographs taken during the compression experiments (Fig. 13b) confirm that shell-lattice structures remain stable at relative densities above 0.2. As anticipated from the simulation results, the response of the $\bar{\rho} = 0.1$ specimen is unstable, i.e. the deformation localizes within a narrow band at the unit-cell level. In the photographs shown in Fig. 13c, the void phase of the specimen becomes apparent as black spots within those unit-cells that experienced the highest deformation.

The yield strengths are estimated through a 0.2%-offset definition using the theoretical elastic modulus. All experimental results (black open triangles in Fig. 10a) fall within 5% of the estimated initial yield values. Black open triangles are also included in Fig. 12a to show the experimentally-measured plastic dissipation at 30% strain next to the simulation results. For the largest relative densities ($\bar{\rho} = 0.3$ and 0.4), these measurements fall within 3% of the numerically predicted ones.

Table 3

β - values for the “iso-shell” geometries obtained. The computed Zener ratios are presented to validate their elastic isotropy.

	Density	0.01	0.02	0.05	0.1	0.2	0.3	0.4	0.5
β [-]		0.325	0.35	0.375	0.375	0.4	0.375	0.375	0.375
ζ [-]		1.015	0.996	0.983	1.026	0.998	1.011	0.997	0.990

Table 4

Coordinates of approximate solution for a 9×9 node grid for $\beta = 0.375$.

	1	2	3	4	5	6	7	8	9
1	[0.0000]	[0.0710]	[0.1401]	[0.2050]	[0.2635]	[0.3134]	[0.3517]	[0.3760]	[0.3844]
	[1.0000]	[1.0000]	[1.0000]	[1.0000]	[1.0000]	[1.0000]	[1.0000]	[1.0000]	[1.0000]
	[0.3634]	[0.3571]	[0.3381]	[0.3067]	[0.2635]	[0.2094]	[0.1457]	[0.0748]	[0.0000]
2	[0.0000]	[0.0714]	[0.1406]	[0.2056]	[0.2643]	[0.3145]	[0.3534]	[0.3787]	[0.3887]
	[0.9692]	[0.9731]	[0.9756]	[0.9766]	[0.9761]	[0.9739]	[0.9699]	[0.9638]	[0.9546]
	[0.3657]	[0.3588]	[0.3393]	[0.3077]	[0.2643]	[0.2101]	[0.1464]	[0.0753]	[0.0000]
3	[0.0000]	[0.0723]	[0.1421]	[0.2075]	[0.2668]	[0.3179]	[0.3585]	[0.3866]	[0.4017]
	[0.9385]	[0.9462]	[0.9511]	[0.9532]	[0.9522]	[0.9478]	[0.9398]	[0.9276]	[0.9093]
	[0.3724]	[0.3637]	[0.3430]	[0.3105]	[0.2668]	[0.2124]	[0.1485]	[0.0769]	[0.0000]
4	[0.0000]	[0.0740]	[0.1446]	[0.2107]	[0.2709]	[0.3237]	[0.3671]	[0.4000]	[0.4236]
	[0.9077]	[0.9193]	[0.9267]	[0.9297]	[0.9282]	[0.9217]	[0.9097]	[0.8915]	[0.8639]
	[0.3841]	[0.3721]	[0.3492]	[0.3153]	[0.2709]	[0.2163]	[0.1521]	[0.0796]	[0.0000]
5	[0.0000]	[0.0764]	[0.1484]	[0.2154]	[0.2770]	[0.3321]	[0.3796]	[0.4191]	[0.4549]
	[0.8789]	[0.8924]	[0.9022]	[0.9063]	[0.9043]	[0.8956]	[0.8796]	[0.8553]	[0.8185]
	[0.4011]	[0.3843]	[0.3582]	[0.3224]	[0.2770]	[0.2219]	[0.1572]	[0.0834]	[0.0000]
6	[0.0000]	[0.0797]	[0.1535]	[0.2220]	[0.2854]	[0.3436]	[0.3963]	[0.4443]	[0.4950]
	[0.8461]	[0.8655]	[0.8778]	[0.8829]	[0.8804]	[0.8695]	[0.8495]	[0.8191]	[0.7732]
	[0.4244]	[0.4009]	[0.3705]	[0.3322]	[0.2854]	[0.2296]	[0.1641]	[0.0884]	[0.0000]
7	[0.0000]	[0.0841]	[0.1603]	[0.2308]	[0.2968]	[0.3589]	[0.4179]	[0.4759]	[0.5418]
	[0.8154]	[0.8386]	[0.8533]	[0.8595]	[0.8565]	[0.8434]	[0.8194]	[0.7829]	[0.7278]
	[0.4547]	[0.4226]	[0.3870]	[0.3454]	[0.2968]	[0.2398]	[0.1731]	[0.0947]	[0.0000]
8	[0.0000]	[0.0897]	[0.1695]	[0.2430]	[0.3124]	[0.3792]	[0.4452]	[0.5137]	[0.5907]
	[0.7846]	[0.8117]	[0.8289]	[0.8361]	[0.8325]	[0.8174]	[0.7893]	[0.7467]	[0.6824]
	[0.4918]	[0.4508]	[0.4092]	[0.3636]	[0.3124]	[0.2534]	[0.1844]	[0.1022]	[0.0000]
9	[0.0000]	[0.0968]	[0.1822]	[0.2608]	[0.3349]	[0.4068]	[0.4788]	[0.5545]	[0.6371]
	[0.7538]	[0.7848]	[0.8044]	[0.8127]	[0.8086]	[0.7913]	[0.7592]	[0.7105]	[0.6371]
	[0.5330]	[0.4865]	[0.4400]	[0.3902]	[0.3349]	[0.2718]	[0.1983]	[0.1103]	[0.0000]

The experimentally determined SEA at 30% engineering strain is 7.3, 10.5, 13.2 and 15.3 J/g for the $\bar{\rho} = 0.1$, 0.2, 0.3 and 0.4 specimens, respectively.

The Young's modulus estimates fall within 30% of the theoretical values. However, these are not presented as a model validation since the experiments were not designed for measuring elastic properties. As described in Bonatti and Mohr (2017), the combination of cyclic elastic loading along with local optical strain measurements appears to be more appropriate for obtaining reliable Young's modulus estimates from experiments on porous metamaterials.

5.2. Results for elastically-isotropic shell-lattices

5.2.1. Numerical identification of an elastically-isotropic topology

The evolution of elastic properties for the shell-structures with β -values spanning the range $0.2 \leq \beta \leq 5$ is computed to identify elastically-isotropic structures. Fig. 7d presents the evolution of the Zener anisotropy ratio as a function of β for a relative density of $\bar{\rho} = 0.3$; the graph crosses the isotropy line ($\zeta = 1$) at $\beta \approx 0.38$. Our subsequent work focuses on this particular family of elastically-isotropic shell lattices (“iso-shells”). The β values achieving elastic isotropy are presented in Table 3 as a function of the relative density. The mesh coordinates for a 9×9 grid corresponding to $\beta = 0.375$ (isotropic case for most relative densities considered) are given in Table 4.

5.2.2. Scaling of stiffness and plastic dissipation

Fig. 14a, b present the scaling of the Young's and bulk moduli as a function of the relative density. The comparison with the results for the TPMS-like lattices (blue curves) reveals that the Young's modulus of the iso-shells (black line) of equal density is always higher than the mean stiffness of the TPMS-like structures (Fig. 14a). It is also always higher than the stiffness of optimal isotropic truss-lattices (dashed line) and exceeds 60% of the Hashin-Shtrikman bound for relative densities greater than 10%. The bulk stiffness of the iso-shell is also close to that of the TPMS-like structures for relative

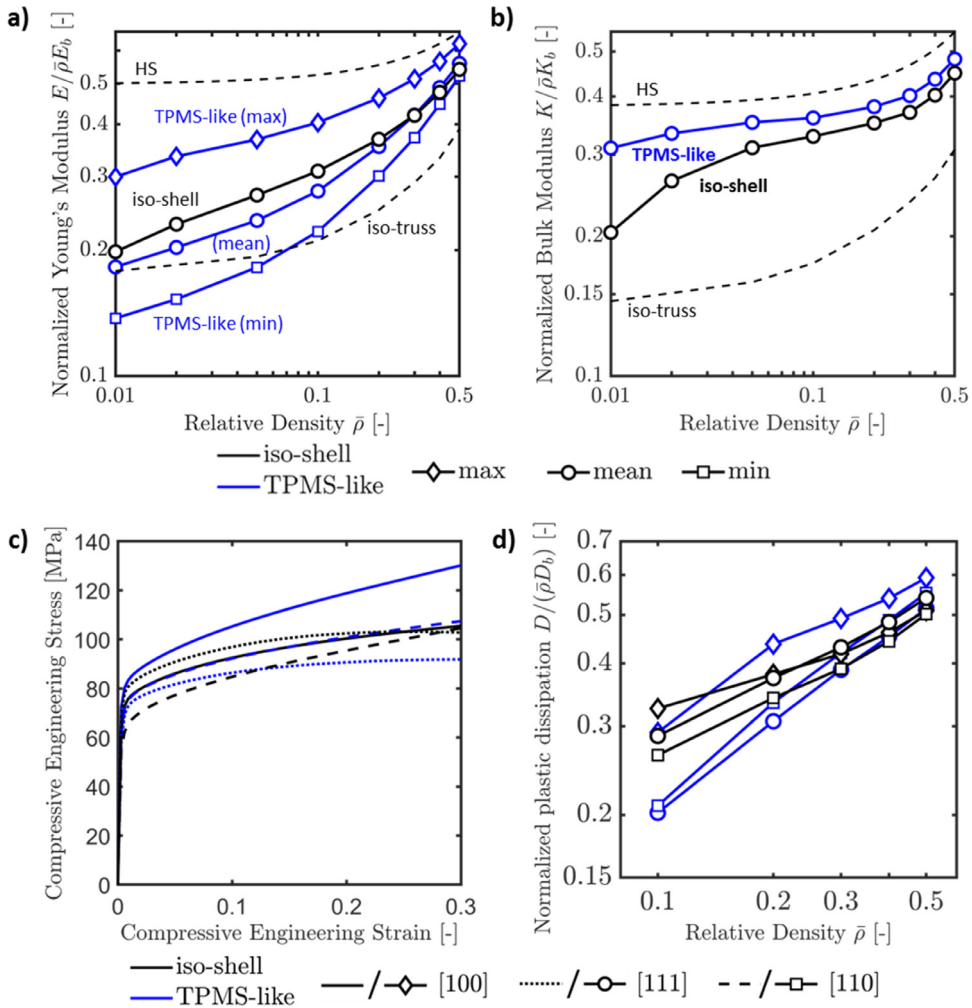


Fig. 14. Comparison of mechanical performance of anisotropic TPMS-like shell-lattices and the iso-shell structures: a) Young's modulus, and b) bulk modulus; dashed curves in a) and b) represent the response of optimal plate-lattices (HS bound) and optimal isotropic truss-lattices; c) direction-dependent stress-strain curves for uniaxial compression of structures of 30% relative density. d) direction-dependent energy absorption under uniaxial compression. (For interpretation of the references to color in this figure legend, the reader is referred to the web version of this article.)

densities greater than 10%, while it proves less stiff at low relative densities (Fig. 14b). The distribution of directional uniaxial yield stress is provided for $\bar{\rho} = 0.01$ in Fig. 9c, with [100] and [111] the strongest directions while [110] is the weakest. The max-to-min ratio of yield stresses (1.28) is reduced as compared to the TPMS-like structure (1.4).

Fig. 14c depicts the monotonically-increasing stress-strain response of an iso-shell structure of 30% relative density for uniaxial compression along three different lattice directions (black curves). Even though elastic-isotropy does not imply plastic isotropy, we observe a substantially reduced plastic anisotropy as compared to the TPMS-like structure (blue curves). For example, at a compressive strain of 0.2, the stress level varies by $\pm 5\%$ for the iso-shell, while variations of $\pm 18\%$ are seen for the TPMS-like structure.

The reduced plastic anisotropy of the iso-shell also becomes apparent when comparing its plastic dissipation per unit volume (for compressive strains of up to 0.3) to that of the TPMS-like structures (Fig. 14d). The three black curves for the iso-shell are much closer to one-another than those of the TPMS-like structure (the respective max-to-min ratios are 1.11 and 1.31 for a relative density of $\bar{\rho} = 0.2$). While the curves for the iso-shell are sandwiched between the curves for the strongest and weakest directions of the TPMS-like structures at relative densities greater than 20%, its plastic dissipation for loading along the [100] direction is even higher than that of the TPMS-like structure at a relative density of 10%.

5.2.3. Experimental validation of large deformation response

The manufactured iso-shell and TPMS-like specimens all had a measured relative density of about 28%. Quasi-static experiments with two repetitions are performed along the [100] and [111] directions. The recorded engineering stress versus engineering strain curves are shown in Fig. 15a. Both structures show a stress-plateau ($\partial\sigma/\partial\varepsilon \approx 0$) at around 15% strain when loaded along the [111] direction. For the [111] direction specimens, we also observe the band-type localization of defor-

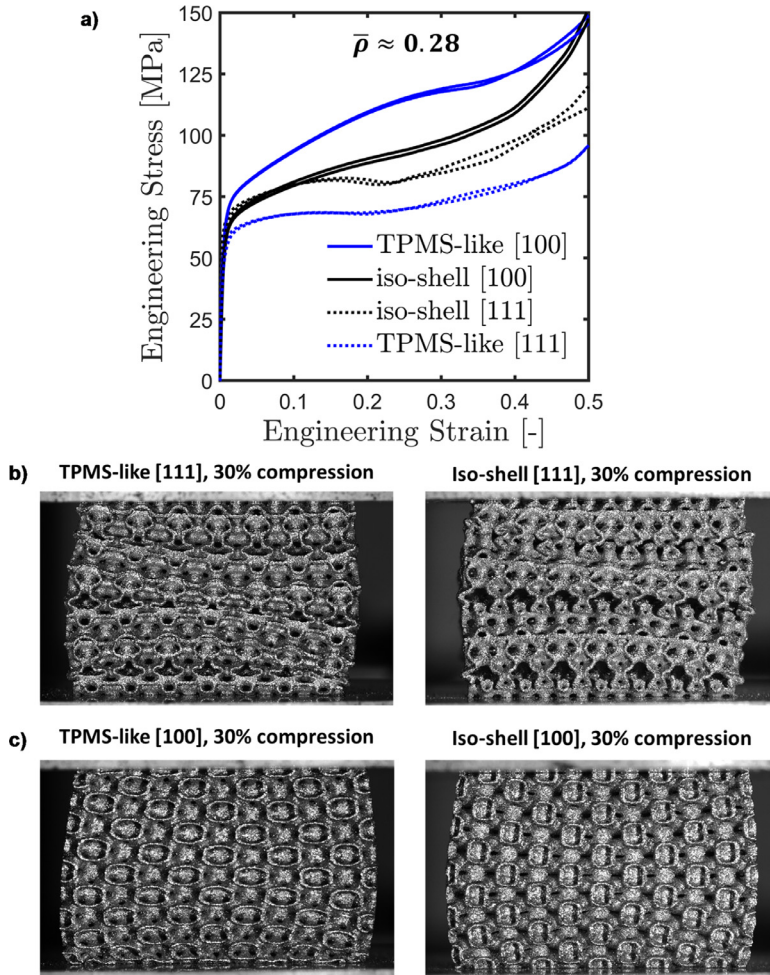


Fig. 15. a) Comparison of the measured stress-strain response of TPMS-like and iso-shell structures under uniaxial compression along [100] and [111] directions at about 28% relative density. b) Deformed [111]-specimens compressed to an engineering strain of 30% for the TPMS-like (left) and elastically-isotropic (right) shell-lattices. c) Corresponding deformed [100]-specimens.

mation at the macroscopic level as reflected by the non-periodic surface patterns in the photographs of the specimens at 30% strain (Fig. 15b). The [100] specimens show a more uniform deformation pattern at the specimen surface (Fig. 15c) and positive strain hardening ($\partial\sigma/\partial\varepsilon > 0$) throughout the entire experiment (solid curves in Fig. 15a). As in the numerical simulations, we observe a lower degree of anisotropy in the stress-strain response for the iso-shell specimens than for the TPMS-like specimens. In particular, the elasto-plastic response of the iso-shell is almost the same for the [100] and [111] specimens for engineering strains of up to 15%. The two repeats per testing scenario fall on top of each other, confirming the robustness of the manufacturing and experimental procedures.

5.3. Analysis of the cell wall material: results and discussion

The stress-strain curve for the cell wall material is determined from compression experiments on triangular honeycomb specimens (Fig. 6c). Based on the measured force history $F(t)$ and the logarithmic axial strain ε_a (determined through surface DIC), the true axial stress in the cell wall material is computed,

$$\sigma_a = \frac{F}{\bar{\rho}A_0} \exp(\varepsilon_a), \quad (14)$$

with the initial macroscopic cross-sectional area A_0 and the relative density $\bar{\rho}$. The identified stress-strain curve is shown by solid dots in Fig. 16a. It is in reasonable agreement with the red stress-strain curve that has been derived from the manufacturer-provided data and used in all numerical simulations. The blue curve in Fig. 16a depicts the true strain-strain curve obtained from testing the specimens extracted from 1.5 mm thick stainless steel 316L sheets. The particular feature of the additively-manufactured stainless steel 316L is that it displays a significantly higher yield point than conventional sheets with the same alloy composition. This yield strength advantage vanishes as the material is deformed. Due to the

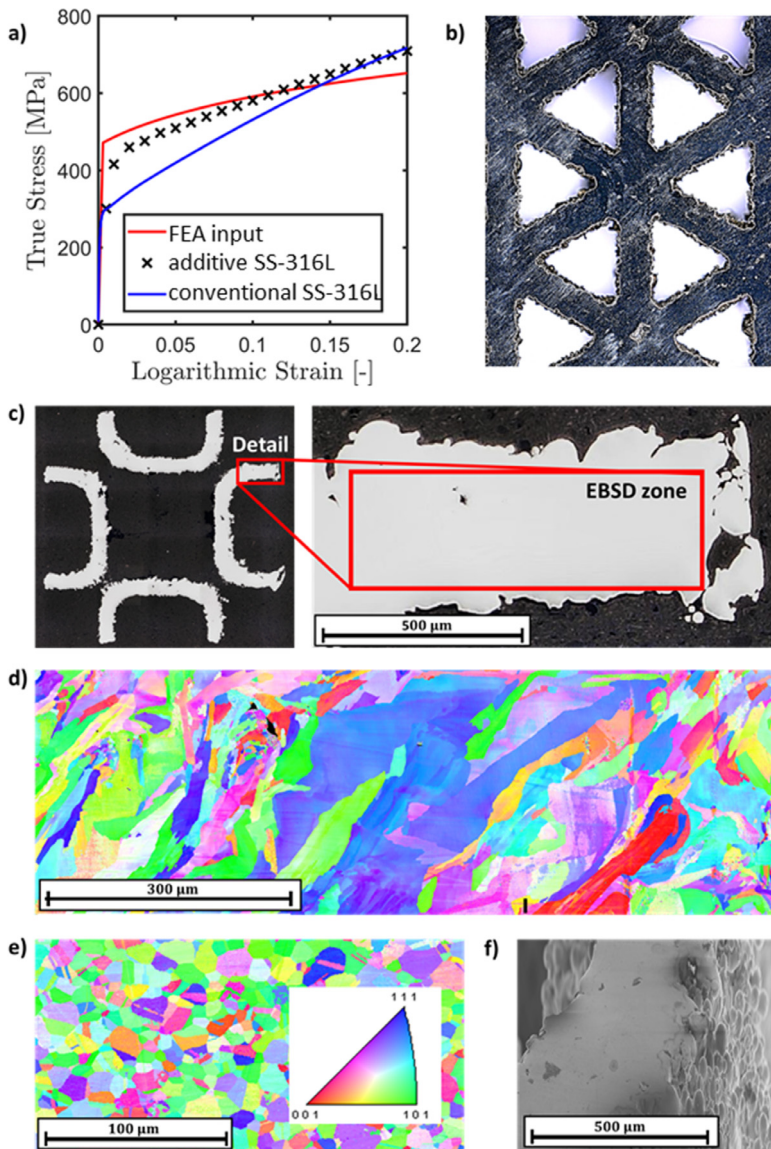


Fig. 16. a) Experimentally-measured stress–strain curves for additively- and conventionally-manufactured stainless steel 316; b) cross-section of a triangular honeycomb specimen; c) view of the cell-wall of a shell-lattice specimen; d) inverse pole figure obtained through EBSD analysis on a cell wall of an additively-manufactured shell-lattice specimen, and e) for a conventionally-manufactured 316 L stainless steel sheet; f) cell wall of a shell-lattice specimen showing surface roughness and balling effect. (For interpretation of the references to color in this figure legend, the reader is referred to the web version of this article.)

lower hardening of the additively-manufactured material, the two stress–strain curves (black dots and blue curve) cross at a true strain of about 0.2. The observed higher yield strength is in line with the results from previous studies on additively-manufactured stainless steel (e.g. Hanzl et al., 2015; Suryawanshi et al., 2017; Wang et al., 2018).

EBSD analysis is performed to gain further insight into the difference between additively-manufactured and rolled stainless steel. The inverse pole figure for a cell wall region of about $300 \times 900 \mu\text{m}^2$ (Fig. 16c, d) shows a highly heterogeneous microstructure with large variations in grain size (ranging from smaller than $1 \mu\text{m}$ to more than $100 \mu\text{m}$) and grain aspect ratios (ranging from 1 to greater than 10). The corresponding inverse pole figure for the sheet material (Fig. 16e) is very different: a uniform microstructure is observed with predominantly equi-axed grains with grain sizes in the range of $5\text{--}30 \mu\text{m}$. As discussed by Suryawanshi et al. (2017), the refinement of additively-manufactured microstructures due to the high cooling rates during manufacturing is one source of strengthening. However, when comparing the microstructures shown in Fig. 16d and e, refined grains are only seen in small regions. The strengthening can thus not be exclusively attributed to a Hall-Petch effect associated with the EBSD-identified grain sizes. Microstructures with highly unconventional grain shapes and sizes spanning several orders of magnitude have also been observed in additively-manufactured stainless steels by Wang et al. (2018). They argued that solute strengthening and low-angle grain boundaries contribute to the increased

yield strength in additively-manufactured stainless steel 316L. Furthermore, they emphasize the potential of strengthening in additively-manufactured stainless steel due to subgrain level structures such as solidification cells.

The microscopic images also show the surface roughness of the additively-manufactured specimens. It is characterized by irregular creases of a depth of about 50 μm (Fig. 16b). The surface roughness is partly due to a balling effect, with powder particles attached to the cell wall edges (Fig. 16f). Defects in the form of porosity near the center of the cell wall intersections are also visible on the polished cross-section of the honeycomb specimen shown in Fig. 16b.

6. Conclusions

Smooth shell structures of FCC symmetry are obtained by locally smoothening the geometry of thin-walled hollow octet trusses. Even though the surfaces are defined through a function that minimizes the total curvature, the resulting basic surface turns out to be similar to a Triply-Periodic Minimal Surface (TPMS). In a first step, we compare the effective mechanical properties of the TPMS-like shell-lattice with those of the widely-used octet truss-lattice. Paying special attention to anisotropy, the elastic stiffness, yield strength and the large deformation response of these metamaterial structures is determined through detailed finite element simulations for relative densities ranging from 1% to 50%. Both structures display an important anisotropy with max-to-min stiffness ratios of up to 2 as a function of the direction of loading. The results reveal that the mechanical properties of the shell-lattices are almost always superior to those of the stretching-dominated octet truss-lattices of equal mass. In particular, the shell-lattices outclass the octet trusses in terms of plastic dissipation ($\bar{\rho} > 0.1$). For example, at a relative density of 20%, the energy absorption (under compression) of the TPMS-like shell-lattice is 80% higher than that of an octet truss-lattice of the equal mass when comparing the strongest and weakest directions.

Within the proposed family of smooth shell-lattices, we also identify a special geometry which exhibits an isotropic elastic response at the macroscopic level. Our computational results show that its Young's modulus is always higher than that of optimal isotropic truss-lattices and approaches the Hashin-Shtrikman bound at high relative densities. As compared to the TPMS-like architecture, the elastically-isotropic shell-lattice also features a significantly reduced plastic anisotropy, a property that is preserved even at large strains. The computational results are confirmed through compression experiments on additively-manufactured stainless steel 316L shell-lattice specimens. An important byproduct of our experimental work on the 400 μm thick cell wall material is the observation that the additively-manufactured stainless steel exhibits a significantly higher yield strength than conventional 316L sheets.

The good mass-specific mechanical properties observed for high relative densities along with the absence of discrete joints make the anisotropic and isotropic shell-lattices a strong candidate for hierarchical designs. Their open structure also allows the shell-lattices to be fabricated using powder-bed and liquid bath based additive manufacturing techniques, as opposed to the closed-cell structure of plate-lattices. From the point of view of multi-functionality, it is worth noting that the shell-lattices have the particularity of separating two fluid phases of approximately equal volume which is of interest to (heat-, chemical-) exchanger applications.

Acknowledgments

Thank are due to Thomas Tancogne-Dejean (MIT), Professor Tomasz Wierzbicki (MIT) and Dr. Christian Roth (ETH) for valuable discussions. Professor Pavel Hora (ETH) and Dr. Christian Rith are thanked for their support of our experimental work. The partial financial support of the MIT/ETH Industrial Fracture Consortium and the Swiss National Science Foundation project SNF 200021-165939 is gratefully acknowledged.

Supplementary materials

Supplementary material associated with this article can be found, in the online version, at [doi:10.1016/j.jmps.2018.08.022](https://doi.org/10.1016/j.jmps.2018.08.022).

Appendix. Comparison of macroscopic stress-strain response of shell-lattices based on smooth shell surfaces with $\beta = 1$ and Triply Periodic Minimal Surfaces (TPMS)

Although the family of shell-lattices developed herein are derived from a bending-energy inspired potential that minimizes total curvature, the basic structure obtained for $\beta = 1$ resembles to a Triply Periodic Minimal Surface (TPMS) known as "Schoen F-RD". In this Appendix, we explore the similarities and differences of those structures in terms of mechanical behavior. In order to obtain meshes for the TPMS Schoen F-RD, the same procedure as for the bending-energy inspired shell-lattices is reproduced where the objective function is changed to

$$\int_{\Omega} (k_1 - k_2)^4 dA.$$

Numerical simulations are conducted for the F-RD shell-lattices as described in detail for the other structures in the main document.

A view of both structures is presented in Figs. S1a and S1b. The TPMS shell-lattice (Fig. S1b) presents flat sections along with steep saddle points, while the bending-energy inspired shell-lattice (Fig. S1a) is smoothly curved throughout. Both

structures present a similar level of anisotropy, as well as similar directional Young's moduli at all relative densities from 0.01 to 0.5 (Fig. S1c). A maximum relative difference of 6% is observed at relative density 0.1. The same is true of both structures' bulk moduli (maximum relative difference of 8%) with in each case the F-RD shell-lattice over-performing the $\beta = 1$ shell-lattice slightly. The comparison of both materials' response to large strain loadings shows this ranking reversed. While preserving similar levels of anisotropy and very similar responses overall, the $\beta = 1$ structure provides slightly higher macroscopic stress-levels in the cases investigated. Fig. S1e and f provide evidence of such findings for uniaxial compression at relative densities of 0.2 and 0.5, respectively. Fig. S1g and h compare the equivalent plastic strain distribution for both structures at relative density 0.2, under uniaxial compression in the [100] direction. At an engineering strain of 0.3, the $\beta = 1$ structure displays a smoother distribution of plastic dissipation ($\bar{\varepsilon}_{max}^p = 0.63$), as the F-RD shell-lattice presents concentration zones around the saddle points in which curvature is concentrated, with a notably higher peak in equivalent plastic strain ($\bar{\varepsilon}_{max}^p = 0.94$).

References

- Abueidda, D.W., Dalaq, A.S., Abu Al-Rub, R.K., Jasiuk, I., 2015. Micromechanical finite element predictions of a reduced coefficient of thermal expansion for 3D periodic architected interpenetrating phase composites. *Compos. Struct.* 133, 85–97. doi:[10.1016/j.compstruct.2015.06.082](https://doi.org/10.1016/j.compstruct.2015.06.082).
- Al-Ketan, O., Adel Assad, M., Abu Al-Rub, R.K., 2017. Mechanical properties of periodic interpenetrating phase composites with novel architected microstructures. *Compos. Struct.* 176, 9–19. doi:[10.1016/j.compstruct.2017.05.026](https://doi.org/10.1016/j.compstruct.2017.05.026).
- Berger, J.B., Wadley, H.N.G., McMeeking, R.M., 2017. Mechanical metamaterials at the theoretical limit of isotropic elastic stiffness. *Nature* 543, 533–537. doi:[10.1038/nature21075](https://doi.org/10.1038/nature21075).
- Bobbert, F.S.L., Lietaert, K., Eftekhari, A.A., Pouran, B., Ahmadi, S.M., Weinans, H., Zadpoor, A.A., 2017. Additively manufactured metallic porous biomaterials based on minimal surfaces: A unique combination of topological, mechanical, and mass transport properties. *Acta Biomater.* 53, 572–584. doi:[10.1016/j.actbio.2017.02.024](https://doi.org/10.1016/j.actbio.2017.02.024).
- Bonatti, C., Mohr, D., 2017. Large deformation response of additively-manufactured FCC metamaterials: From octet truss lattices towards continuous shell mesostructures. *Int. J. Plast.* 92, 122–147. doi:[10.1016/j.ijplas.2017.02.003](https://doi.org/10.1016/j.ijplas.2017.02.003).
- Carlton, H.D., Lind, J., Messner, M.C., Volkoff-Shoemaker, N.A., Barnard, H.S., Barton, N.R., Kumar, M., 2017. Mapping local deformation behavior in single cell metal lattice structures. *Acta Mater.* 129, 239–250. doi:[10.1016/j.actamat.2017.02.023](https://doi.org/10.1016/j.actamat.2017.02.023).
- Dalaq, A.S., Abueidda, D.W., Abu Al-Rub, R.K., 2016a. Mechanical properties of 3D printed interpenetrating phase composites with novel architected 3D solid-sheet reinforcements. *Compos. Part A Appl. Sci. Manuf.* 84, 266–280. doi:[10.1016/j.compositesa.2016.02.009](https://doi.org/10.1016/j.compositesa.2016.02.009).
- Dalaq, A.S., Abueidda, D.W., Abu Al-Rub, R.K., Jasiuk, I.M., 2016b. Finite element prediction of effective elastic properties of interpenetrating phase composites with architected 3D sheet reinforcements. *Int. J. Solids Struct.* 83, 169–182. doi:[10.1016/j.ijsolstr.2016.01.011](https://doi.org/10.1016/j.ijsolstr.2016.01.011).
- Deshpande, V.S.S., Fleck, N.A.A., Ashby, M.F.F., 2001a. Effective properties of the octet-truss lattice material. *J. Mech. Phys. Solids* 49, 1747–1769. doi:[10.1016/S0022-5096\(01\)00010-2](https://doi.org/10.1016/S0022-5096(01)00010-2).
- Deshpande, V.S., Ashby, M.F., Fleck, N.A., 2001b. Foam topology: bending versus stretching dominated architectures. *Acta Mater.* 49, 1035–1040. doi:[10.1016/S1359-6454\(00\)00379-7](https://doi.org/10.1016/S1359-6454(00)00379-7).
- Elsayed, M.S.A.A., Pasini, D., 2010. Multiscale structural design of columns made of regular octet-truss lattice material. *Int. J. Solids Struct.* 47, 1764–1774. doi:[10.1016/j.ijsolstr.2010.03.003](https://doi.org/10.1016/j.ijsolstr.2010.03.003).
- Gurtner, G., Durand, M., 2014. Stiffest elastic networks. *Proc. R. Soc. A Math. Phys. Eng. Sci.* 470, 20130611–20130611. doi:[10.1098/rspa.2013.0611](https://doi.org/10.1098/rspa.2013.0611).
- Han, S.C., Lee, J.W., Kang, K., 2015. A new type of low density material: shellular. *Adv. Mater.* 27. doi:[10.1002/adma.201501546](https://doi.org/10.1002/adma.201501546), n/a-n/a.
- Hanzl, P., Zetek, M., Bakša, T., Kroupa, T., 2015. The influence of processing parameters on the mechanical properties of SLM parts. *Procedia Eng.* 100, 1405–1413. doi:[10.1016/j.proeng.2015.01.510](https://doi.org/10.1016/j.proeng.2015.01.510).
- Hashin, Z., Shtrikman, S., 1963. A variational approach to the theory of the elastic behaviour of multiphase materials. *J. Mech. Phys. Solids* 11, 127–140. doi:[10.1016/0022-5096\(63\)90060-7](https://doi.org/10.1016/0022-5096(63)90060-7).
- He, Z.Z., Wang, F.C., Zhu, Y.B., Wu, H.A., Park, H.S., 2017. Mechanical properties of copper octet-truss nanolattices. *J. Mech. Phys. Solids* 101, 133–149. doi:[10.1016/j.jmps.2017.01.019](https://doi.org/10.1016/j.jmps.2017.01.019).
- Kapfer, S.C., Hyde, S.T., Mecke, K., Arns, C.H., Schröder-Turk, G.E., 2011. Minimal surface scaffold designs for tissue engineering. *Biomaterials* 32, 6875–6882. doi:[10.1016/j.biomaterials.2011.06.012](https://doi.org/10.1016/j.biomaterials.2011.06.012).
- Lambert, C.A., Radzilowski, L.H., Thomas, E.L., 1996. Triply periodic level surfaces as models for cubic tricontinuous block copolymer morphologies. *Philos. Trans. Math. Phys. Eng. Sci.* 354, 2009–2023. doi:[10.1098/rsta.1996.0089](https://doi.org/10.1098/rsta.1996.0089).
- Lee, D.W., Khan, K.A., Abu Al-Rub, R.K., 2017. Stiffness and yield strength of architected foams based on the Schwarz primitive triply periodic minimal surface. *Int. J. Plast.* 95, 1–20. doi:[10.1016/j.ijplas.2017.03.005](https://doi.org/10.1016/j.ijplas.2017.03.005).
- Lee, J.-H., Wang, L., Boyce, M.C., Thomas, E.L., 2012. Periodic Bicontinuous Composites for High Specific Energy Absorption. *Nano Lett.* 12, 4392–4396. doi:[10.1021/nl302234f](https://doi.org/10.1021/nl302234f).
- Maldovan, M., Ullal, C.K., Jang, J.H., Thomas, E.L., 2007. Sub-micrometer scale periodic porous cellular structures: microframes prepared by holographic interference lithography. *Adv. Mater.* 19, 3809–3813. doi:[10.1002/adma.200700811](https://doi.org/10.1002/adma.200700811).
- Meza, L.R., Zelhofer, A.J., Clarke, N., Mateos, A.J., Kochmann, D.M., Greer, J.R., 2015. Resilient 3D hierarchical architected metamaterials. *Proc. Natl. Acad. Sci. U.S.A.* 112, 11502–11507. doi:[10.1073/pnas.1509120112](https://doi.org/10.1073/pnas.1509120112).
- Mohr, D., 2005. Mechanism-based multi-surface plasticity model for ideal truss lattice materials. *Int. J. Solids Struct.* 42, 3235–3260. doi:[10.1016/j.ijsolstr.2004.10.032](https://doi.org/10.1016/j.ijsolstr.2004.10.032).
- O'Masta, M.R., Dong, L., St-Pierre, L., Wadley, H.N.G., Deshpande, V.S., 2017. The fracture toughness of octet-truss lattices. *J. Mech. Phys. Solids* 98, 271–289. doi:[10.1016/j.jmps.2016.09.009](https://doi.org/10.1016/j.jmps.2016.09.009).
- Suryawanshi, J., Prashant, K.G., Ramamurthy, U., 2017. Mechanical behavior of selective laser melted 316L stainless steel. *Mater. Sci. Eng. A* 696, 113–121. doi:[10.1016/j.msea.2017.04.058](https://doi.org/10.1016/j.msea.2017.04.058).
- Tancogne-Dejean, T., Mohr, D., 2018a. Stiffness and specific energy absorption of additively-manufactured metallic BCC metamaterials composed of tapered beams. *Int. J. Mech. Sci.* 141, 101–116. doi:[10.1016/j.ijmecsci.2018.03.027](https://doi.org/10.1016/j.ijmecsci.2018.03.027).
- Tancogne-Dejean, T., Mohr, D., 2018b. Elastically-isotropic elementary cubic lattices composed of tailored hollow beams. *Extrem. Mech. Lett.* 22, 13–18. doi:[10.1016/j.eml.2018.04.005](https://doi.org/10.1016/j.eml.2018.04.005).
- Tancogne-Dejean, T., Diamantopoulou, M., Gorji, M.B., Bonatti, C., Mohr, D., 2018c. 3D plate-lattices: An emerging class of low-density metamaterial exhibiting optimal isotropic stiffness. *Adv. Mater.* 180334. doi:[10.1002/adma.20180334](https://doi.org/10.1002/adma.20180334).
- Thomas, E.L., Anderson, D.M., Henkee, C.S., Hoffman, D., 1988. Periodic area-minimizing surfaces in block copolymers. *Nature* 334, 598–601. doi:[10.1038/334598a0](https://doi.org/10.1038/334598a0).
- Wang, L., Lau, J., Thomas, E.L., Boyce, M.C., 2011. Co-continuous composite materials for stiffness, strength, and energy dissipation. *Adv. Mater.* 23, 1524–1529. doi:[10.1002/adma.201003956](https://doi.org/10.1002/adma.201003956).
- Wang, Y.M., Voisin, T., McKeown, J.T., Ye, J., Calta, N.P., Li, Z., Zeng, Z., Zhang, Y., Chen, W., Roehling, T.T., Ott, R.T., Santala, M.K., Depond, P.J., Matthews, M.J., Hamza, A.V., Zhu, T., 2018. Additively manufactured hierarchical stainless steels with high strength and ductility. *Nat. Mater.* 17, 63–70. doi:[10.1038/NMAT5021](https://doi.org/10.1038/NMAT5021).

- Wendy Gu, X., Greer, J.R., 2015. Ultra-strong architected Cu meso-lattices. *Extrem. Mech. Lett.* 2, 7–14. doi:[10.1016/j.eml.2015.01.006](https://doi.org/10.1016/j.eml.2015.01.006).
- Xiong, J., Mines, R., Ghosh, R., Vaziri, A., Ma, L., Ohrndorf, A., Christ, H.-J., Wu, L., 2015. Advanced micro-lattice materials. *Adv. Eng. Mater.* 17, 1253–1264. doi:[10.1002/adem.201400471](https://doi.org/10.1002/adem.201400471).
- Zheng, X., Smith, W., Jackson, J., Moran, B., Cui, H., Chen, D., Ye, J., Fang, N., Rodriguez, N., Weisgraber, T., Spadaccini, C.M., 2016. Multiscale metallic metamaterials. *Nat. Mater.* 1–8. doi:[10.1038/nmat4694](https://doi.org/10.1038/nmat4694).